

## Computational Neuroscience

## The impact of denoising on independent component analysis of functional magnetic resonance imaging data

Jean Michel Pignat<sup>a,b,\*</sup>, Oleksiy Koval<sup>b</sup>, Dimitri Van De Ville<sup>c,d</sup>, Sviatoslav Voloshynovskiy<sup>b</sup>, Christoph Michel<sup>a</sup>, Thierry Pun<sup>b</sup><sup>a</sup> Division of Neurology, Department of Clinical Neurosciences, University of Geneva, Geneva University Hospitals, CH-1211 Geneva 14, Switzerland<sup>b</sup> Department of Informatics, University of Geneva, CH-1227 Carouge-Geneva, Switzerland<sup>c</sup> Institute of Bioengineering, Ecole polytechnique Fédérale de Lausanne, CH-1015 Lausanne, Switzerland<sup>d</sup> Department of Radiology and Medical Informatics, CH-1211 Geneva 14, Switzerland

## HIGHLIGHTS

- ▶ Preprocessing utility in ICA has not previously been demonstrated.
- ▶ We prove the strong necessity for preprocessing in preparation for ICA.
- ▶ Low-pass filtering parameters are needed to improve ICA.
- ▶ Simple Gaussian smoothing is as efficient than more complex denoising methods.
- ▶ Noise reduction seems to have the most effect on increasing component independence.

## ARTICLE INFO

## Article history:

Received 9 August 2011

Received in revised form

16 September 2012

Accepted 20 October 2012

## Keywords:

Independent component analysis

Denoising

Wavelet-based filtering

Non-stationary Gaussian modelling

Gaussian smoothing

## ABSTRACT

Independent component analysis (ICA) is a suitable method for decomposing functional magnetic resonance imaging (fMRI) activity into spatially independent patterns. Practice has revealed that low-pass filtering prior to ICA may improve ICA results by reducing noise and possibly by increasing source smoothness, which may enhance source independence; however, it eliminates useful information in high frequency features and it amplifies low signal fluctuations leading to independence loss. On the other hand, high-pass filtering may increase the independence by preserving spatial information, but its denoising properties are weak. Thus, such filtering strategies did not lead to simultaneous enhancements in independence and noise reduction; therefore, band-pass filtering or more sophisticated filtering methods are expected to be more appropriate.

We used advanced wavelet filtering procedures, such as wavelet-based methods relying upon hard and soft coefficient thresholding and non-stationary Gaussian modelling based on geometrical prior information, to denoise artificial and real fMRI data. We compared the performance of these methods with the performance of traditional Gaussian smoothing techniques.

First, we demonstrated both analytically and empirically the consistent performance increase of spatial filtering prior to ICA using spatial correlation and statistical sensitivity as quality measures. Second, all filtering methods were computationally efficient. Finally, denoising using low-pass filters was needed to improve ICA, suggesting that noise reduction may have a more significant effect on the component independence than the preservation of information contained within high frequencies.

© 2012 Elsevier B.V. All rights reserved.

## 1. Introduction

Functional magnetic resonance imaging (fMRI) is a non-invasive technique based on blood oxygen level-dependent (BOLD) effects

(Ogawa et al., 1990) that provides information on the spatiotemporal dimensions of brain functions. Various statistical methods have been developed to extract BOLD signals from fMRI data (Lange et al., 1999). Among such methods are univariate procedures, including time–frequency analyses (Mittra et al., 1997), correlation-based methods (Bandettini et al., 1993), and ANOVA-like approaches, as the widely used statistical parametric mapping (SPM) (Friston et al., 1994; Friston, 1995). These approaches share common inherent weaknesses because they do not define the intrinsic structure of the haemodynamic response. Additionally, they require prior

\* Corresponding author at: Division of Neurology, Geneva University Hospitals, rue Gabrielle-Perret-Gentil 4, CH-1211 Geneva 14, Switzerland.  
Tel.: +41 223823527; fax: +41 223723705.

E-mail address: [jean-michel.pignat@hcuge.ch](mailto:jean-michel.pignat@hcuge.ch) (J.M. Pignat).

assumptions regarding the fMRI signal statistics, and they ignore the relationships among voxels.

To overcome these drawbacks, multivariate methods, such as principal component analysis (PCA) (Moeller and Strother, 1991) or independent component analysis (ICA) (Comon, 1994), represent elegant alternatives. McKeown, followed by Calhoun, demonstrated the applicability of spatial (McKeown et al., 1998; Calhoun and Adali, 2006) and temporal (Calhoun et al., 2001b, 2003) ICA models to fMRI data for which the fundamental theorems of identifiability, separability, and uniqueness could be ensured (Comon, 1994; Eriksson and Koivunen, 2003, 2004). Moreover, ICA modelling does not impose constraints on the model in that spatial and temporal patterns of brain activity are statistically independent, follow non-Gaussian distributions, and are mixed together (McKeown and Sejnowski, 1998; Hyvärinen and Oja, 2000; Hyvärinen et al., 2001).

BOLD effects are small with 1–5% signal changes for 1.5 Tesla MRI data (Bullmore et al., 1999) and are corrupted by noise and other artefacts stemming from a variety of sources (Edelstein et al., 1986). The signal-to-noise ratio (SNR) of fMRI data, therefore, is low and the potential for inaccurate ICA results is non-negligible. Although ICA incorporates denoising techniques by isolating the noisy independent components and by reducing the data through initial PCA processing, practice has shown that prior spatial filtering improves ICA (Hyvärinen and Oja, 2000; Calhoun et al., 2001a; Hyvärinen et al., 2001; Khullar et al., 2011). Alternatively, Li proposed an iterative filtering–projection operation on the source sample space to achieve a feature-selective ICA (Li et al., 2007). In this light, it is also worthwhile to mention a recent study that investigated group-level ICA and the influence of inter-subject variability (Allen et al., 2012).

Because we are interested in denoising tools that act on the spatial dimensions, we focused our interest on a spatial ICA model. Low-pass and high-pass filtering may be proposed to enhance ICA performance. Low-pass filters, such as Gaussian smoothing, are simple though computationally efficient denoisers. Because active spatial sources in fMRI are assumed to be localized and smooth due to vascular point spread functions that produce local correlations (Malonek et al., 1997; Calhoun et al., 2001a), we hypothesize that enhanced source smoothness may increase source independence. However, such denoisers simultaneously eliminate high frequency features containing information that is useful for estimating the (de)mixing matrix and amplify low signal fluctuations, which leads to independence loss (Hyvärinen et al., 2001). By contrast, high-pass frequency filters preserve spatial information that may contribute to increases in the independence, but their denoising properties are weak (Hyvärinen et al., 2001). Accordingly, the best filtering effects may be obtained using filtering methods that increase the independence and reduce the noise. Such effects are expected from band-pass filters and wavelet-based techniques (Hyvärinen et al., 2001). However, the utility of prior filtering has previously been only qualitatively characterized (Calhoun et al., 2001a) and within the context of a novel integrated wavelet-based framework, ICA was applied in the wavelet domain and performance of this scheme was only compared to prior smoothing (Khullar et al., 2011). Hence, a systematic analysis assessing the utility of prior denoising and the performance of various denoising methods is lacking. Therefore, we applied conventional Gaussian smoothing techniques to data prior to ICA and compared the results with those of two different wavelet-based denoising techniques. Although MRI data are corrupted by Rician noise that is multiplicative (Gudbjartsson and Patz, 1995; Sijbers et al., 1998; Wink and Roerdink, 2004, 2006), it is now understood that Rician noise becomes Gaussian inside MR brain images (Gudbjartsson and Patz, 1995; Wink and Roerdink, 2006). The first technique tested was a wavelet routine that performs

coefficient thresholding in the transform domain, with applications to biomedical imaging that have been widely discussed in the literature (Ruttimann et al., 1998; Alexander et al., 2000; Turkheimer et al., 2000; Zaroubi and Goelman, 2000; Ghugre et al., 2003). The second method tested for comparison employed a novel stochastic image model based on a non-stationary Gaussian modelling within the Bayesian framework. This method uses geometrical image prior information derived from the local image structure in the non-decimated wavelet domain (Voloshynovskiy et al., 2005). Benchmarking demonstrated the best efficiency with respect to processing standard images in a comparison with the best denoising methods (Pignat et al., 2005). Its denoising properties respect local information, thereby preserving local image features. This technique may be suitable for ICA.

Thus, the main purposes of this paper are (1) to demonstrate analytically and empirically the strong necessity for denoising prior to ICA and (2) to define the best filtering method, as determined by ICA performance. We expect that the identification of filtering parameters will improve ICA and may reveal which data features principally influence ICA.

The rest of the paper is organized as follows. The first section is divided into two parts. The first part presents the ICA and demonstrates the applicability of filtering prior to ICA; the second part describes the three denoising methods: the simple Gaussian smoothing and two more sophisticated techniques based on the wavelet transform in conjunction with shrinkage and non-stationary Gaussian modelling. Procedures for generating simulated noisy data are described in Section 2. The results are presented in Section 3. The spatial denoising efficiency of all filtering methods was quantified in terms of the signal-to-noise ratio (SNR). Subsequently, spatiotemporal correlations and statistical classification criteria were applied to the resulting statistical ICA map and ICA time course. Finally, Section 4 concludes the paper with a discussion of results.

## 2. Theory

### 2.1. ICA modelling

The main goal of linear ICA models for fMRI analysis is to link component maps and their time courses to the acquired fMRI data.  $X_{t,v}$ , with  $t = 1, 2, \dots, T$  and  $v = 1, 2, \dots, V$ , is a matrix that represents the observed fMRI images, where  $V$  is the number of voxels placed individually in separated columns and  $T$  are the rows of the time series for each voxel  $v$ .  $S_{k,v}$ ,  $k = 1, 2, \dots, K$ , is the set of statistically independent sources, with  $K$  the number of independent components placed in one row. Hence,  $X_{t,v}$  results from the linear mixing of a set of statistically independent sources  $S_{k,v}$  with a mixing matrix  $A_{t,k}$ . In matrix form, the ICA model for fMRI data becomes:

$$X = AS. \quad (1)$$

ICA identifies a demixing matrix  $W_{k,t}$  such that the independent components in each row of  $\hat{S}_{k,v}$  (which approximates  $S$ ) can be deduced from the following demixing expressions (Egolf et al., 2004):

$$\hat{S} = WX \quad (2)$$

and

$$X = W^{-1}\hat{S}. \quad (3)$$

$W$  is a square matrix of full rank such that the inverse  $W^{-1}$  exists and  $W^{-1} = A$  when  $\hat{S} \rightarrow S$ .

In this paper, the implementation of ICA is based on the principle of maximizing the statistical independence of the estimated components using Infomax (Bell and Sejnowski, 1995; Hyvärinen

et al., 2001), which maximizes the joint entropy or information flow. In information theory, a set of independent random variables with a uniform joint probability density function has maximum joint entropy, and the random variables are mutually independent (Cover and Thomas, 2006). Therefore, the principal goal of Infomax is to seek the demixing matrix  $W$  that maximizes the entropy of  $\hat{S}$ ,  $H(\hat{S})$  (Egolf et al., 2004):

$$H(\hat{S}) = \frac{1}{N} \sum_{k=1}^N \ln(p_{\hat{S}}(\hat{S}^k)). \quad (4)$$

For a more detailed presentation of Infomax, see Stone (2004).

## 2.2. Analytical applicability

ICA decomposes signals corresponding to independent sources by separating a signal of interest from artefacts and other noisy components. This explains why, in theory, prior filtering is not necessary, although filtering has proven to be useful in practice. Hyvärinen demonstrated the applicability of filtering on one-dimensional data (Hyvärinen et al., 2001). We present here an analytical extension that may be applied to fMRI images.

According to the convolution theorem, multiplication in the transform domain (Fourier, Wavelet, etc.) is equivalent to convolution in the initial domain. Thus, filtering of  $X_{t,v}$  to give  $X'_{t,v}$  corresponds to multiplying  $X_{t,v}$  from the right by a matrix  $M_{v,v}$  such that, in matrix form:

$$X' = XM = ASM = AS', \quad (5)$$

so,

$$X' = AS', \quad (6)$$

where  $S'$  represents the denoised independent components.

The same filtering matrix  $M$  is applied to the mixtures  $X$  and to the independent components  $S$ . Otherwise, the components in  $S'$  are not mixed with each other because the matrix  $M$  is, by definition, a component-wise filtering matrix. Because the mixing matrix  $A$  remains unchanged after filtering,  $W$  may be estimated and applied to the original data  $X$  to obtain the independent components. Once prior filtering is analytically validated, the question remains as to why data denoising is useful and which type of filtering methods should be applied.

## 2.3. Practical applicability

Two reasons may underlie the expected benefits of prior spatial filtering. Because the noise of  $X$  perturbs estimation of the demixing matrix  $W$  during entropy maximization, denoising preprocessing steps improve the identification of source components. Secondly, BOLD sources are assumed to be smooth. Therefore, we hypothesize that enhancing the smoothness of the data may increase the independence of BOLD sources by maximizing the uniform distribution of the sources, which leads to a higher joint entropy.

Low-pass filters, which act as smoothers, can be strong denoisers (Worsley et al., 1996) and improve the estimation of the demixing matrix and source independence. However, they also suppress the spatial details encoded in the high-frequency components that are necessary for estimating the demixing matrix. Low-pass filters do not take into account fine-grained local information in the data, such as the juxtaposition of flat regions, textures, and edges. Hence, non-active bordering areas become correlated with the haemodynamic sources, thereby blurring the source borders and hampering detection precision.

By contrast, high-pass frequency filters preserve source independence by reducing slow fluctuations and by keeping the useful high frequency details. Nevertheless, they remain weak denoisers

and yield poor improvements in the estimation of the demixing matrix.

An ideal filtering method would be one that increases the independence of the components while removing noise, meaning that it should provide a compromise between low- and high-pass filtering (Hyvärinen and Oja, 2000; Hyvärinen et al., 2001). Wavelet-based methods using shrinkage, particularly non-stationary Gaussian modelling within Bayesian frameworks, may have the prerequisite denoising profiles.

## 3. Materials and methods

### 3.1. Filtering methods

#### 3.1.1. Gaussian smoothing

A Gaussian filter is, by definition, a linear low-pass frequency filter that convolves fMRI images with a Gaussian kernel defined by a Gaussian function. Gaussian filters increase the SNR by removing noise, as stated in the matched-filter theorem (Rosenfeld and Kak, 1982; Worsley et al., 1996). Elimination of the high frequency components of noise, where most of the white noise signal energy is concentrated, leads to SNR improvement. The smoothing strength can be numerically controlled by adjusting the full width at half-maximum (FWHM) of the Gaussian. A broad panel of Gaussian kernels was applied to measure the efficiency of these filters. Several statistical packages for neuroimaging analysis propose this filtering method (Gold et al., 1998). Gaussian denoising is also at the heart of the Statistical Parametric Mapping (SPM) software package (Wellcome Department of Imaging Neuroscience, London UK, <http://www.fil.ion.ucl.ac.uk/spm/>).

#### 3.1.2. Wavelet-based denoising by wavelet domain thresholding

Rician noise in MR images follows a Gaussian distribution in practice. Therefore, wavelet-based filtering methods that assume white Gaussian noise (WGN) have been developed in the past several years due to their analytical strength and wide applicability in the biomedical domains. The application of spatial wavelet transforms exploits the sparsity of data representations in the wavelet domain, which improves the robustness of modelling (Ruttimann et al., 1998; Turkheimer et al., 2000; Van De Ville et al., 2004). Hence, denoising schemes by wavelet domain thresholding have been developed. For many reasons, spline bases (Unser, 1999) possess optimal properties for approximating biomedical images: they have the smallest L2 error and they are well-localized in both the time and frequency domains due to their smoothness. Moreover, fractional spline wavelets (Blu and Unser, 2000; Unser and Blu, 2000) are particularly useful because they are symmetric and orthonormal. Indeed, symmetric wavelets avoid the introduction of phase distortions between different decomposition levels (Turkheimer et al., 1999), and orthonormal wavelets transform white noise into white noise (Hilton et al., 1996). Denoising has been pursued using schemes based on thresholding detail coefficients in the wavelet domain. They are characterized by the amount of smoothness inserted into the denoised image (Blu and Unser, 2000; Unser and Blu, 2000).

In this paper, we used the *spm-wavelet* software (Wink and Roerdink, 2004). This software includes the *fractional spline wavelet* package (Blu and Unser, 2000; Unser and Blu, 2000), which constructs symmetric orthonormal spline wavelets of real-valued degree, and the *Wavelab* package (Buckheit and Donoho, 1995), which contains various schemes for wavelet-based denoising by hard and soft thresholding of wavelets coefficients and by other shrinkage methods (Donoho and Johnstone, 1994, 1995). For each scheme, we applied a broad range of wavelet-level decompositions,

spline real-valued degrees and progressive thresholds of wavelet coefficients according to the Oracle principle.

### 3.1.3. Non-stationary Gaussian modelling based on geometrical prior information in the wavelet domain

Based on the accepted assumption that MRI noise is Gaussian, we present here a new denoising method developed by Voloshynovskiy et al. (2005). This technique uses a stochastic image model based on prior geometrical information regarding the local structure of the image in the critically sampled and non-decimated wavelet transform domain. Because real images are non-stationary, they proposed to split the image into several non-overlapping subregions that could be modelled as locally stationary; the local variance of each subregion could then be estimated using an adaptive maximum likelihood estimator. Because the filtering performance was enhanced in the wavelet domain, they applied a partition technique and an adaptive local variance estimation in the transform domain. To avoid the Gibbs phenomenon, a non-decimated wavelet transform without downsampling was used (Chrysafis, 2000). In addition, the authors developed a novel algorithm that preserves the denoising performance of their method without enhancing the computational complexity: this is the so-called edge process modelling, which decreases residual correlations in the high frequencies. This algorithm also takes into account the differences in the local statistics within each subregion: it treats flat areas as non-stationary zero-mean Gaussian, and edge regions as locally stationary non-zero mean Gaussian with very low variance. In terms of the spatial SNR, the denoising performance was demonstrated on fMRI data in comparison with the wavelet transforms and Gaussian smoothing (Pignat et al., 2005, 2007).

Denoising strength can be modulated by two parameters: the size of the selected subregion and the prior noise variance introduced during computation of the Bayesian estimate in the local subband. A range of window sizes for delimiting the subregion and a wide panel of progressive noise standard deviations (SD) were used in our study. This method is developed in the appendix.

## 3.2. Data and experience

### 3.2.1. Data

Artificial data that simulate multiple brain activity in space and in time, were chosen for a quantitative comparison of the effects of filtering on ICA, because the time series and some of their statistical characteristics, as noise variance, SNR, or BOLD size, could be previously defined. To avoid uniform flat regions with low voxel amplitudes in which Rician noise may be estimated using a Rayleighian distribution rather than a Gaussian distribution (Gudbjartsson and Patz, 1995; Wink and Roerdink, 2006), a full brain template comprising different BOLD regions was preferable to isolated BOLD areas. To approach a realistic situation and to validate the ICA results obtained with the synthetic data, analysis was extended across hybrid data corresponding to real echo-planar images (EPI) acquired during rest; several regions of interest (ROI) were then selected onto which various simulated haemodynamic function were added.

**3.2.1.1. Artificial data.** The BrainWeb Simulator (Kwan et al., 1996) was used to generate a 3D noise-free template that corresponded to a T2\*-weighted MR brain image with the following parameters: modalities, T2; image size, 185 × 217 voxels of 1 mm × 1 mm × 1 mm; noise, 0%; and intensity nonuniformity, 0%. We selected slice 108, which held the right inverted omega shape of the precentral gyrus (radiological orientation), and data segmentation was carried out by SPM. Because wavelet denoising prefers square images of power 2, the template was reduced to 128 × 128

voxels and partially centred on the right inverted omega shape of the precentral gyrus, giving a new template image  $T(v)$ , where  $v$  denotes the voxel location.  $T(v)$  was repeated 80 times to form a constant time-series template,  $T(v, t)$ , in which  $t$  is the time index of the voxel  $v$ . Including the inverted omega shape, we defined four cortical BOLD ROIs of 579, 529, 402, and 369 voxels respectively, and one empty rectangular area of 500 voxels inside the white matter; these five ROIs were labelled  $f_r(v)$  and indexed by  $r = \{1, 2, 3, 4, 5\}$ . Between ROIs 2 and 3,  $f_2(v)$  and  $f_3(v)$ , we delimited an area of intersection containing 190 voxels, where the activity of both ROIs was afterwards superimposed. For easy reference, the five regions of interest are named thereafter as follows: aROI1, aROI2, aROI3, aROI4 and aROI5 (Fig. 1a–e). From each ROI a binary BOLD mask,  $M_r(v)$ , was created. Constant time-series of  $f_r(v)$  was labelled  $f_r(v, t)$ .

We used the convoluted binary meander time course proposed by the Vanderbilt web page (former <http://www.vuiis.vanderbilt.edu/fmriphantoms/>) (Pickens et al., 2005) to generate a haemodynamic response function (HRF) with the following temporal parameters: period of 20 scans, 1 scan per second (s), maximum amplitude of 1, onset delay (OD), 1 s, time to pick (TP), 6 s, and FWHM, about 9 s. This reference HRF (HRF1) was then modulated to create two additional HRFs (HRF2 and HRF3) with different temporal characteristics: OD of 7 and 0 s respectively, TP of 6 s for both, and FWHM, about 8 and 6.8 s, respectively. We generated also a default-mode activity with the same duration (HRF4), represented by a low frequency (0.025 Hz) sine wave (Cordes et al., 2001) of one cycle (40 scans) and of maximum amplitude of 1. The HRFs and the sine sequence were then repeated 4 and 2 times, respectively, to obtain 4 different time series of 80 scans,  $h_s(t)$  with index  $s = \{1, 2, 3, 4\}$ . Matched by indexes, such as  $r = s$  giving  $u = r = s$  for  $r, s = \{1, 2, 3, 4\}$ , HRFs and the time series of the first four ROIs were then superimposed, by adding  $h_u(t)$  on each voxel of  $f_u(v, t)$ . Because brain activation measured by fMRI corresponds to a signal change of 1–5%, we multiplied the HRFs by appropriate factors,  $p_u$ , so that the peak of  $h_s(t)$  corresponded to an increase of 5% and 4% against the baseline of each BOLD voxel, for  $f_2(v, 1)$  and for  $f_{1,3,4}(v, 1)$ , respectively (Fig. 1a–e):

$$f_u(v, t) = f_u(v, 1) + \left( h_u(t) \frac{p_u f_u(v, 1)}{100} \right) = f_u(v, 1) \left( 1 + \frac{p_u h_u(t)}{100} \right); \quad (7)$$

it is worth noting that the time course inside the intersection of aROI1 and aROI2, was elicited by their respective HRF, using a linear convolution model (Fig. 1a–c). Finally, we took aROI5 as a ventricular space (Fig. 1e), inside which cerebrospinal fluid was modelled by a Brownian motion based on a Wiener process in space and time.

The final noise-free template time-series containing all ROIs time course,  $F_0(v, t)$ , was then defined as

$$F_0(v, t) = \begin{cases} f_u(v, t), & \text{inside the BOLD regions,} \\ T(v, t), & \text{otherwise.} \end{cases} \quad (8)$$

Before proceeding to the corruption of  $F_0(v, t)$  with noise, two realizations,  $Z_1(v)$  and  $Z_2(v)$ , of independent and identically distributed Gaussian noise  $Z_1, Z_2 \sim N(0, \sigma_z^2)$  with zero-mean and known variance, were generated. We repeated  $Z_1(v)$  and  $Z_2(v)$  80 times following a first-order autoregressive AR(1) process with  $\rho = 0.5$ , to obtain correlated time-series:

$$Z_1(v, t) = \rho Z_1(v, t - 1) + \varepsilon(v, t) \quad (9)$$

and

$$Z_2(v, t) = \rho Z_2(v, t - 1) + \varepsilon(v, t) \quad (10)$$

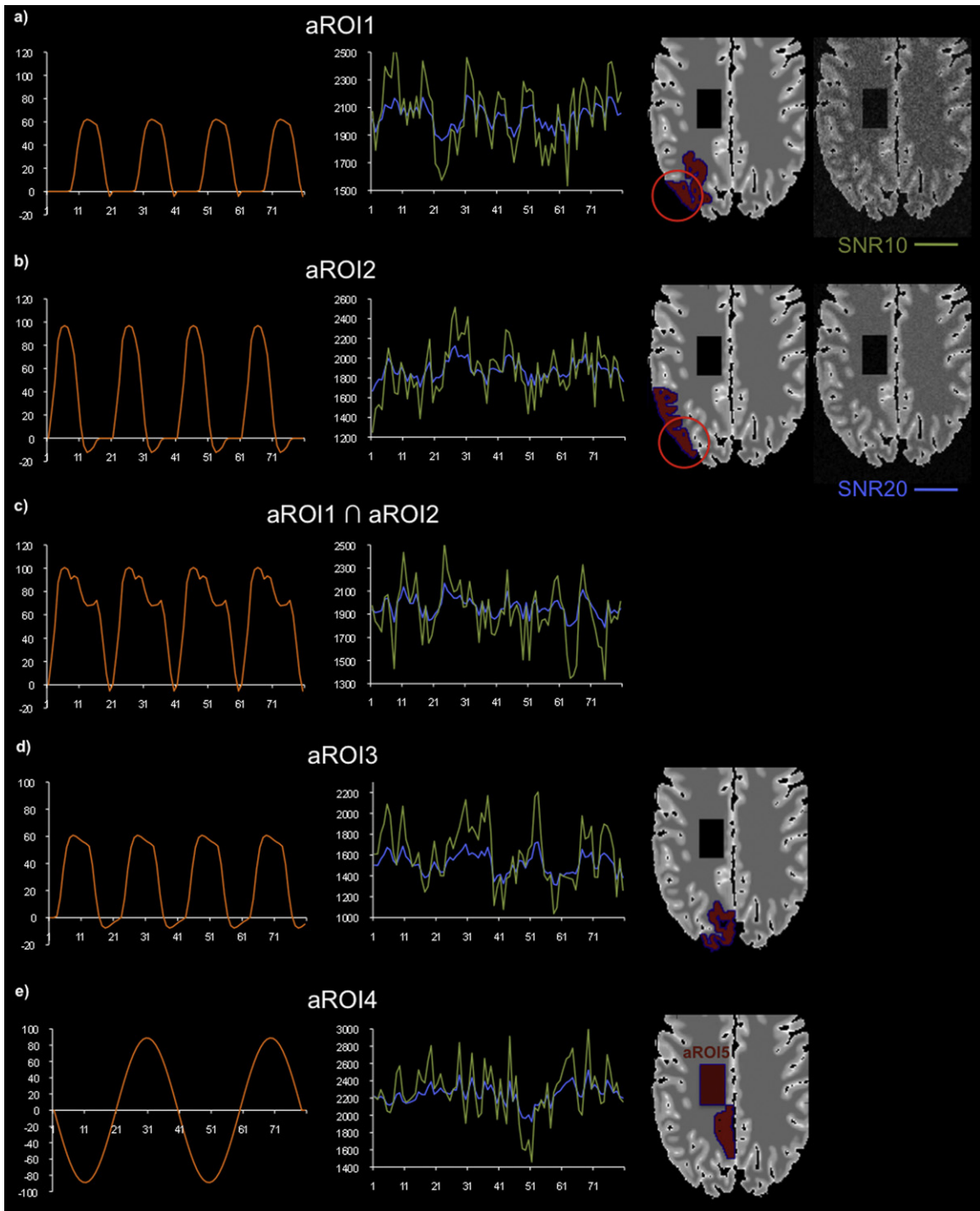


**Fig. 1.** The noise-free image template with the BOLD ROIs shown in red and their respective HRF template: the left chart shows the real time series of one voxel within the BOLD area and the right chart the same time series degraded by Rician noise of 10 dB (green) and of 20 dB (blue). (a) aROI1: ROI1 with superimposed HRF1 (peak increase of 4% against the baseline); image template degraded by Rician noise of 10 dB (extreme right). (b) aROI2: ROI2 with superimposed HRF2 (peak increase of 5% against the baseline); image template degraded by Rician noise of 20 dB (extreme right). (c) Time course inside the intersection of aROI1 and aROI2 (red circle), elicited by their respective HRF, using a linear convolution model. (d) aROI3: ROI3 with superimposed HRF3 (peak increase of 4% against the baseline). (e) aROI4: ROI4 with superimposed HRF4 (peak increase of 4% against the baseline); representation of aROI5 inside the image template (BOLD: blood oxygen level-dependent; aROI: region of interest within the artificial data; HRF: haemodynamic response function). (For interpretation of the references to colour in this figure legend, the reader is referred to the web version of the article.)

where  $\varepsilon$  is a white noise process,  $\varepsilon \sim \mathcal{N}(0, \sigma_\varepsilon^2)$ . Introduction of white Rician noise in a 2D noise-free image,  $X(v)$ , could be computed as (Gudbjartsson and Patz, 1995; Wink and Roerdink, 2004)

$$\tilde{X}(v) = \sqrt{(X(v) + Z_1(v))^2 + Z_2(v)^2}. \quad (11)$$

The Rician distributed noise in this created noisy image has a SD that can be approximated as

$$\sigma_R \cong \sigma_Z \sqrt{2 - \frac{\pi}{2}} \quad (12)$$

(Gudbjartsson and Patz, 1995; Wink and Roerdink, 2004).

This method was applied to our time-series template,  $F_0(v, t)$ , for degradation purposes, and a noisy correlated time-series template,  $F_1(v, t)$  was obtained as

$$F_1(v, t) = \sqrt{(F_0(v, t) + Z_1(v, t))^2 + Z_2(v, t)^2}. \quad (13)$$

The SNR was defined prior to generating the noisy template time-series. From the standpoint of improving the efficiency of the preprocessing filtering function, we selected two different SNRs: a low SNR of 10 dB (Fig. 1a), for which ICA could not detect the active BOLD regions, and a higher SNR of 20 dB (Fig. 1b), for which at least one BOLD area could be detected by ICA without denoising. We used the following formula to calculate the SNR of our noisy data with  $t = 1$  and  $v = V$  corresponding to all voxels for time 1, such that  $F_1^1 = F_1(V, 1)$ , with the noise-free original data,  $F_0^1 = F_0(V, 1)$ :

$$\text{SNR}_{F_1^1} = 20 \log_{10} \frac{\sigma_{F_0^1}}{\sigma_1} = 20 \log_{10} \frac{\sigma_{F_0^1}}{\sigma_{F_1^1 - F_0^1}}, \quad (14)$$

where  $\sigma_1$  is the SD of the noise of the image calculated after subtracting  $F_0^1$  from  $F_1^1$ .

Because the SD of the noise-free data,  $\sigma_{F_0^1}$ , is known, both SNRs were computed with iterative changes in  $\sigma_2$  until the expected SNR values of 10 dB and 20 dB were reached. Subsequently, the obtained variance,  $\sigma_z$  ( $\sigma_z = 230.92$  for SNR = 10 dB) and  $\sigma_z = 71.97$  for SNR = 20 dB, was used to generate all other noisy time-series data,  $F_1^t = F_1(v, t)$  (Fig. 1a–e),  $\forall t$  such that  $t \in \{2, 3, 4, \dots, 80\}$ .

Statistical control of the noise was then performed on both  $F_1^1$ . According to the statistical characteristics of the Rician noise in MR images, the noise outside the brain is Rayleigh distributed, while the noise inside the brain approximates a Gaussian distribution (Gudbjartsson and Patz, 1995; Wink and Roerdink, 2006). After subtracting  $F_0^1$  from  $F_1^1$ , we empirically measured the SD of both types of noise: the SDs of the Gaussian noise ( $\sigma_{Z_c}$ ) and of the Rician noise ( $\sigma_{R_c}$ ) were locally calculated inside and outside the brain, respectively. The results were close to the real values,  $\sigma_z$  and  $\sigma_R$  from Eq. (12), proving statistically the consistency of our artificial data corrupted numerically by Rician noise. For the data set with a noise of 10 dB,  $\sigma_{Z_c}$  ( $\sigma_{Z_c} = 229.37$ ) and  $\sigma_{R_c}$  ( $\sigma_{R_c} = 154.12$ ) approached  $\sigma_z$  ( $\sigma_z = 230.92$ ) and  $\sigma_R$  ( $\sigma_R = 151.28$ ) while for the lower noisy data (20 dB),  $\sigma_{Z_c}$  ( $\sigma_{Z_c} = 71.89$ ) and  $\sigma_{R_c}$  ( $\sigma_{R_c} = 48.04$ ) equalled practically  $\sigma_z$  ( $\sigma_z = 71.97$ ) and  $\sigma_R$  ( $\sigma_R = 47.15$ ). As the whole image was used to determine all SNR of the study, we calculated its noise SD  $\sigma_1$ , whose results were 242.91 and 76.82 for the noisy data with a SNR of 10 dB and of 20 dB, respectively.

Finally, the denoised  $F_1(v, t)$  was labelled  $F_2(v, t)$ , where  $\theta$  was the filter function

$$F_2(v, t) = \theta(F_1(v, t)) \quad (15)$$

**3.2.1.2. Hybrid data.** To improve the ICA under conditions that closely resemble real conditions, hybrid data were generated. A resting state data set was collected on a 1.5 Tesla Philips machine, which was configured as followed: EPI GRE, TR/TE/Flip = 2 s/30 ms/80°, FOV = 220 mm, matrix = 128 × 128 × 400 with 1 axial slice, spatial resolution was 1.7 mm × 1.7 mm × 4 mm. We chose slice 8, which contained the right inverted omega shape of the precentral gyrus. The first 15 “dummy” scans were excluded for longitudinal equilibrium, and the 80 subsequent scans were selected.

Including the inverted omega shape, we defined four cortical BOLD ROIs of 157, 153, 84, and 76 voxels respectively; they were labelled  $g_r(v)$  and indexed by  $r = \{1, 2, 3, 4\}$ . For easy reference, the four regions of interest are named thereafter as follows: hROI1, hROI2, hROI3, and hROI4 (Fig. 2). We simulated brain activity in the time series of each ROI by superimposing the same HRF,  $h_r(t)$ , as

for the artificial data, using the same procedure. As the underlying noise and signal could not be controlled, HRF increase of different percentages was used to evaluate ICA performances in various situations. Hence, we multiplied each  $h_r(t)$  by a defined factor such that its peak corresponded to an increase against the baseline of, respectively, 2% for hROI3, 3% for hROI1 and hROI4, and 4% for hROI2 (Fig. 2). It should be recalled that HRF of hROI4 is a sinusoid function of low frequency mimicking a BOLD resting-state activity.

### 3.2.2. Independent component analysis

ICA was performed using the Matlab-based Group ICA of the fMRI Toolbox (GIFT), version 1.3d (<http://icatb.sourceforge.net/gift/>) (Calhoun et al., 2004; Egolf et al., 2004). We chose the Infomax algorithm (Bell and Sejnowski, 1995) because this approach, which implements higher-order statistical information, yielded consistent fMRI data analysis results (Correa et al., 2007). The first 20 independent components were calculated using the default parametrical options. Because Infomax is iterative with a random starting mixing matrix, several independent applications of ICA to a single data stream may produce variable results. Hence, ICA was iteratively applied 10 times to ensure recording of the best results. Spatially independent components were expressed as statistical Z-score activation maps, which indicated the contribution of each voxel to an independent component.

### 3.2.3. Spatial SNR

Compared to conventional methods, wavelet-based filters and non-stationary Gaussian modelling in the wavelet domain provided the best filtering results. The denoising power of each method was measured in terms of the spatial SNR as defined in Eq. (14). First, the SNR indirectly controls the accuracy of the filtering algorithms, and secondly, it permits a comparison of the best denoising parameters with those parameters that optimize the ICA. Hence, we expected to identify the filtering type (low-pass, high-pass, or band-pass) used to ameliorate the ICA performance and the image features that are crucial for ICA. The first scans of the noisy and denoised data were used to calculate the SNR.

### 3.2.4. Statistical criteria

We compared the effectiveness of denoising in the spatial dimension with control of the temporal dimension. Because the independent components are statistical Z-score activation maps, thresholding may be used to define the active brain areas that are statistically related to the BOLD mask. Functional neuroimaging inference tests multiple hypotheses, which leads to classical multiple comparison problems that must be corrected (Genovese et al., 2002). The false discovery rate (FDR) was chosen to control the expected proportion of incorrectly rejected null hypotheses (type I errors) with a significance level of  $\alpha = 0.05$ , thereby giving a corrected value for  $Z$  that was then used to threshold the maps.

The thresholded Z-scores activation maps,  $C_r(v)$ , were then statistically related to their corresponding BOLD masks,  $M_r(v)$ , with the aid of different statistical criteria, such as:

1. the spatial correlation using the following correlation coefficient formula,  $sCC_r$ :

$$sCC_r = \frac{\sum_{i=1}^I \sum_{j=1}^J (M_r(i, j) - \bar{M}_r)(C_r(i, j) - \bar{C}_r)}{\sum_{i=1}^I \sum_{j=1}^J (M_r(i, j) - \bar{M}_r)^2 \sum_{i=1}^I \sum_{j=1}^J (C_r(i, j) - \bar{C}_r)^2} \quad (16)$$

where  $\bar{C}_r$  indicates the mean of the statistical maps,  $\bar{M}_r$  indicates the mean of their related BOLD mask, and  $I, J$ , indicate the

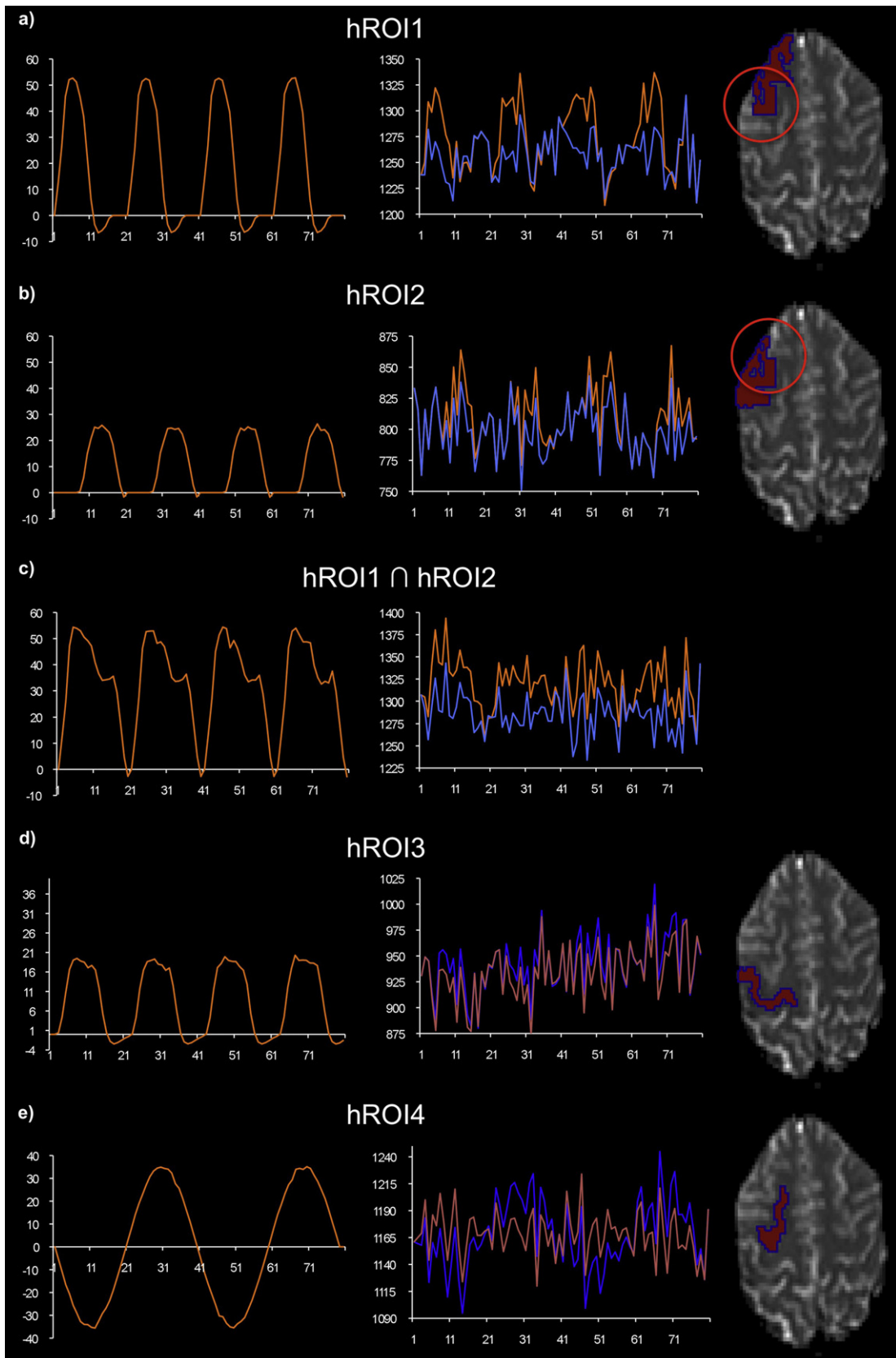


**Fig. 2.** The hybrid data composed of an EPI resting-state template with the selected BOLD ROIs shown in red and their respective HRF template: the right chart shows the real time series of one voxel within the BOLD area (blue) and the same time series with the superimposed HRF template (orange), which is depicted in the left chart. (a) hROI1: ROI1 with superimposed HRF1 (peak increase of 3% against the baseline). (b) hROI2: ROI2 with superimposed HRF2 (peak increase of 4% against the baseline). (c) Time course inside the intersection of hROI1 and hROI2 (red circle), elicited by their respective HRF, using a linear convolution model. (d) hROI3: ROI3 with superimposed HRF3 (peak increase of 2% against the baseline). (e) hROI4: ROI4 with superimposed HRF4 (peak increase of 3% against the baseline). (EPI: echo planar imaging; BOLD: blood oxygen level-dependent; hROI: region of interest within the hybrid data; HRF: haemodynamic response function). (For interpretation of the references to colour in this figure legend, the reader is referred to the web version of the article.)

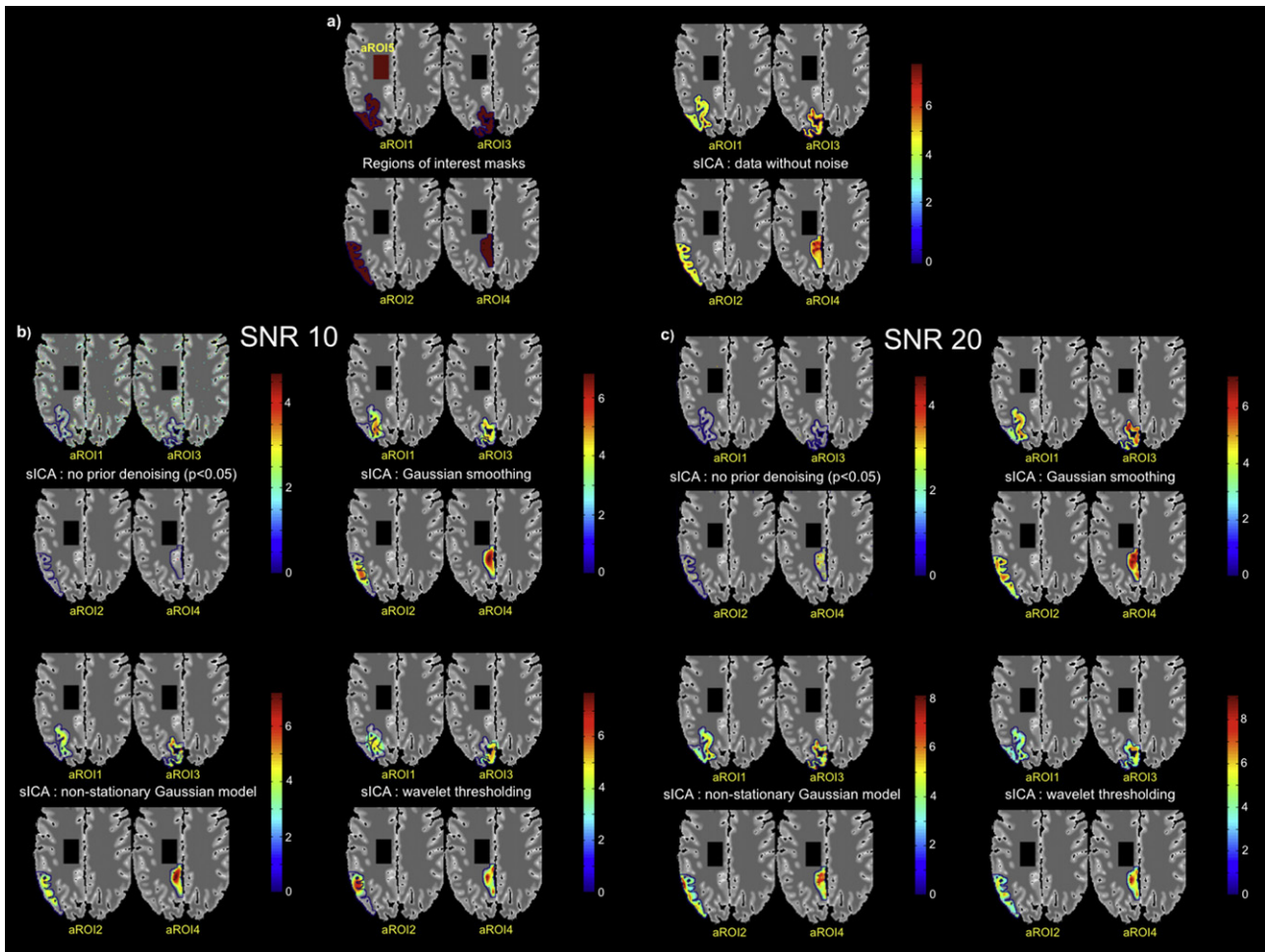


**Fig. 3.** (a) The noise-free image template with the selected BOLD ROIs shown in red (left) and the sICA activation maps from the noise-free template (right). (b) Best sICA activation maps from the data degraded by a Rician noise of 10 dB without prior filtering for a significance level of 0.05 (top left) and after denoising with FDR correction: Gaussian smoothing (top right), filtering with non-stationary Gaussian modelling in the wavelet domain (bottom left), and wavelet denoising by soft thresholding (bottom right). (c) Best sICA activation maps from the data degraded by a Rician noise of 20 dB without prior filtering for a significance level of 0.05 (top left) and after denoising with FDR correction: Gaussian smoothing (top right), filtering with non-stationary Gaussian modelling in the wavelet domain (bottom left), and wavelet denoising by soft thresholding (bottom right). The associated filtering parameters are detailed in Tables 1 and 2 (BOLD: blood oxygen level-dependent; sICA: spatial independent component analysis; FDR: false discovery rate; aROI: region of interest within the artificial data). (For interpretation of the references to colour in this figure legend, the reader is referred to the web version of the article.)

image size. Significance level of  $sCC_r$  was set at  $\alpha = 0.05$ . Only insignificant correlation is mentioned in the results.

- the sensitivity,  $Sn$ , a statistical measure related to the concept of type II error:

$$Sn = \frac{TP}{TP + FN} \quad (17)$$

and the specificity,  $Sp$ , closely linked to the concepts of type I errors,

$$Sp = \frac{TN}{TN + FP} \quad (18)$$

where TP, TN, FN, and FP mean true positive (correct active voxel inside the BOLD area), true negative (correct non active voxel outside the BOLD area), false negative (incorrect non active voxel inside the BOLD area), and false positive (incorrect active voxel outside the BOLD area), respectively.

To strengthen the accuracy of the detection of the real ROIs, we assessed the time correlation between the associated time course,

$h_s(t)$ , of their best Z-map component with its corresponding added HRF time-series:

$$tCC_r = \frac{\sum_{t=1}^T (h_r(t) - \bar{h}_r)(c_r(t) - \bar{c}_r)}{\sqrt{\sum_{t=1}^T (h_r(t) - \bar{h}_r)^2} \sqrt{\sum_{t=1}^T (c_r(t) - \bar{c}_r)^2}} \quad (19)$$

where  $\bar{h}_r$  indicates the mean of the HRF time course and  $\bar{c}_r$  indicates the mean of the best component time series.

As FWHM of the Gaussian smoothing indicates the smoothness grade introduced in the filtered data, we performed for the artificial data a mean square error and a minimal SNR assessment between the image filtered by the latter and the denoised images with both of the wavelet-based methods. The purpose is to provide an equivalent order of the “smoothness” obtained with the wavelet techniques.

## 4. Results

### 4.1. Spatial SNR

For the first set of noisy data (SNR=10 dB), best Gaussian smoothing enhanced the SNR to 10.61 dB for a low FWHM of

**Table 1**

Summary of the best statistical ICA performances in terms of spatial correlation and sensitivity after FDR correction, shown for all aROIs of the artificial data degraded by Rician noise of 10 dB. Inclusion of the sensitivity and of the correlation coefficient that are related to the best spatial correlation and sensitivity respectively. Best result for each aROI is outlined in red and in italic.

	Denoising methods	Filtering parameters	Correlation (FDR)	Related sensitivity	Time correlation	Filtering parameters	Sensitivity (FDR)	Related correlation	Time correlation
<b>aROI1</b>	No denoising		<0.1				<0.1		
	GS	FWHM 21,23,25	<b>0.62</b> (3.05-3.07)	0.49-0.51	0.82	25	<b>0.51</b> (3.05)	0.62	0.82
	NSGM	Window size 28	0.57 (3.2)	0.36	0.89	28,26,30	0.36 (3.02)	0.57	0.89
		Prior noise SD 843.2				843.2,1043.2,1143.2			
	WThr	Spline degree 5				5			
Level decomp 4		0.51 (3.05)	0.42	0.79	4	0.42 (3.05)	0.51	0.79	
Threshold 20					20				
<b>aROI2</b>	No denoising		<0.1				<0.1		
	GS	FWHM 23,24,25	0.65 (3.08-3.09)	0.53	0.87	23,24,25	<b>0.53</b> (3.09)	0.65	0.87
	NSGM	Window size 30	<b>0.66</b> (3.13)	0.50	0.91	30	0.50 (3.13)	0.66	0.91
		Prior noise SD 1043.2				1043.2			
	WThr	Spline degree 5				5			
Level decomp 4		0.58 (3.15-3.16)	0.44	0.89	4	0.44 (3.15-3.16)	0.58	0.89	
Threshold 25,30					25,30				
<b>aROI3</b>	No denoising		<0.1				<0.1		
	GS	FWHM 17-20	0.70 (3.08-3.13)	0.61-0.64	0.90	24,25	<b>0.65</b> (3.07)	0.68	0.88
	NSGM	Window size 34	<b>0.73</b> (3.19)	0.57	0.92	34	0.57 (3.19)	0.73	0.92
		Prior noise SD 643.2				643.2			
	WThr	Spline degree 3				3			
Level decomp 4		0.67 (3.13)	0.56	0.87	4	0.58 (3.12)	0.66	0.89	
Threshold 15					40				
<b>aROI4</b>	No denoising		<0.1				<0.1		
	GS	FWHM 18-23	<b>0.91</b> (3.07-3.10)	0.89-0.90	<0.1	19,22,23	<b>0.90</b> (3.07-3.09)	0.91	<0.1
	NSGM	Window size 26-34	0.88 (3.12-3.15)	0.81-0.82	<0.1	32,30,34	0.82 (3.12-3.15)	0.88	<0.1
		Prior noise SD 1193.2-2143.2				1193.2,1643.2,2043.2			
	WThr	Spline degree 1				5			
Level decomp 3		0.87 (3.12-3.13)	0.80	<0.1	4	0.82 (3.07)	0.84	<0.1	
Threshold 10,14					50				

FDR: false discovery rate; aROI: region of interest in the artificial data; GS: Gaussian smoothing; NSGM: non-stationary Gaussian modelling; WThr: thresholding of wavelet coefficients; FWHM: full width at half maximum; SD: standard deviation.

1 mm, but, as expected, maximal gain was obtained using the different wavelet techniques. Among the thresholding methods that were superior to conventional smoothing techniques, hard thresholding using a wavelet level decomposition 1 and spline degree 1 rendered the best SNR (SNR = 11.45 dB) for a threshold of 2.5. With the same spline and decomposition parameters, SNR after soft thresholding was lower (SNR = 11.4 with a threshold of 1). Moreover, non-stationary Gaussian modelling gave a maximal SNR (SNR = 12.82 dB) for a prior noise of 266.91, while SNR was slightly reduced (SNR = 12.73 dB) with the exact calculated SD of the noise,  $\sigma_I = 242.91$ . A small window of 3 voxels was needed.

With regard to the second set of noisy data (SNR = 20 dB), Gaussian smoothing was not able to improve the SNR (best SNR = 17.46 dB for FWHM = 1 mm), meaning that even with reduced low-pass strength, it mainly eliminated important information from the image. Once more, wavelet-based methods performed the best in terms of denoising. The best SNR (SNR = 20.64 dB) was again obtained using a hard thresholding with wavelet parameters set to 1 for both level and spline degree and for a threshold of 2; soft thresholding could not ameliorate the SNR. Non-stationary Gaussian modelling provided the best results, with a SNR of 22.32 dB, for a prior noise SD of 86.5 and small window size (3 × 3 voxels). Optimal conditions are theoretically achieved for the calculated noise SD  $SD(\sigma_I = 76.82)$ , but the result is slightly lower with a SNR of 22.23 dB for the same window size; this slow SNR difference, also observed for the 10 dB data set, may be explained by the fact that the calculated noise variance estimates the Rician noise, which follows a Rayleighian distribution outside the brain (Gudbjartsson and Patz, 1995; Wink and Roerdink, 2006).

The SNR results suggested several observations: all methods performed optimally in terms of denoising if their parameters were set such that they approximated band-pass rather than low-pass

filters; wavelet-based filters, particularly non-stationary Gaussian modelling, demonstrated superior denoising (Pignat et al., 2005).

## 4.2. Artificial data

### 4.2.1. Artificial data without noise

As a proof of ICA functionality, we first applied it on the noise-free artificial data; results showed the detection of the exact BOLD regions in separated ICA components, except for the Brownian motion inside ROI5 that could not be isolated (Fig. 3a).

### 4.2.2. Artificial data corrupted by noise

As the specificity for the statistical maps of the BOLD regions remained unremarkably high with and without prior denoising ( $Sp > 0.97$ ), the results are therefore not shown. Likewise, ROI5 could not be isolated in a spatial component regardless of the condition (no prior denoising versus prior denoising); hence, its results are neither presented nor discussed in Sections 4.2.2.1 and 4.2.2.2.

**4.2.2.1. Artificial data with a SNR of 10 dB.** Best results for all denoising methods with regard to their optimal filtering parameters, and compared to no prior denoising, are summarized in details in Table 1.

Applied to the noisy data without prior filtering, ICA was unable to detect any activation patterns of the BOLD regions (insignificant correlation for each ROI) even with a low threshold of the Z-score maps ( $\alpha < 0.05$ ) (Fig. 3b).

By contrast, denoising significantly improved the ICA. Gaussian smoothing allowed all BOLD regions to be outlined with application of a progressive FWHM from 5 mm to higher values. The best spatial correlations were obtained using low-pass filtering parameters (FWHM > 16 mm) for all ROIs because the Gaussian kernel covered almost their surface. It is noted that less smoothing strength was needed to detect aROI3 (Fig. 3b).

**Table 2**

Summary of the best statistical ICA performances in terms of spatial correlation and sensitivity after FDR correction, shown for all aROIs of the artificial data degraded by Rician noise of 20 dB. Inclusion of the sensitivity and of the correlation coefficient that are related to the best spatial correlation and sensitivity respectively. Best result for each aROI is outlined in red and in italic.

	Denoising methods	Filtering parameters	Correlation (FDR)	Related sensitivity	Time correlation	Filtering parameters	Sensitivity (FDR)	Related correlation	Time correlation	
aROI1	No denoising		0.03				0.003			
	GS	FWHM 10-14	0.79 (2.99-3.01)	0.69-0.73	0.95	14	0.73 (2.99)	0.79	0.95	
	NSGM	Window size	28-34	0.80 (3.02-3.04)	0.65-0.69	0.95	32,34	0.69 (3.02-3.03)	0.80	0.95
		Prior noise SD	526.9-626.9				576.9,626.9			
	WThr	Spline degree	3			3				
	Level decomp	3	0.79 (3.01)	0.69	0.94	3	0.69 (3.02)	0.79	0.94	
	Threshold	18				18				
aROI2	No denoising		0.27		0.92		0.08		0.92	
	GS	FWHM 6-10	0.88 (2.98-3.02)	0.81-0.84	0.94	10	0.85 (2.98)	0.88	0.94	
	NSGM	Window size	30-34	0.85 (2.99-3.00)	0.79-0.81	0.93	34	0.81 (2.99)	0.85	0.93
		Prior noise SD	626.9				626.9			
	WThr	Spline degree	3			3				
	Level decomp	3	0.83 (3.01)	0.78	0.94	3	0.78 (3.01)	0.83	0.94	
	Threshold	26				26				
aROI3	No denoising		0.21		0.94		0.05		0.94	
	GS	FWHM 8-9	0.90 (3.06-3.07)	0.88-0.89	0.98	12,14	0.90 (3.02-3.03)	0.88	0.98	
	NSGM	Window size	28-34	0.90 (3.09-3.11)	0.80-0.85	0.98	34	0.85 (3.09-3.11)	0.90	0.98
		Prior noise SD	476.9,576.9,626.9				576.9,626.9			
	WThr	Spline degree	1			1				
	Level decomp	3	0.85 (3.05-3.07)	0.83-0.84	0.98	3	0.84 (3.06)	0.85	0.98	
	Threshold	42-90				50				
aROI4	No denoising		0.61		<0.1		0.39		<0.1	
	GS	FWHM 4-7	0.94 (3.08-3.10)	0.93	<0.1	7-9	0.93 (3.08)	0.93-0.94	<0.1	
	NSGM	Window size	26-34	0.94 (3.08-3.16)	0.91-0.93	<0.1	32,34	0.93 (3.09-3.10)	0.94	<0.1
		Prior noise SD	326.9-476.9				326.9,376.9			
	WThr	Spline degree	1,3,5			1				
	Level decomp	2,3	0.93 (3.09-3.10)	0.92-0.93	<0.1	3	0.91 (3.08-3.16)	0.93	<0.1	
	Threshold	17-37,50-98				50-98				

FDR: false discovery rate; aROI: region of interest in the artificial data; GS: Gaussian smoothing; NSGM: non-stationary Gaussian modelling; WThr: thresholding of wavelet coefficients; FWHM: full width at half maximum; SD: standard deviation.

We applied, then, the filter based on non-Gaussian modelling in the wavelet domain. All denoising properties, from low-pass to high-pass filtering, were evaluated using several subregion sizes (firstly sizes of  $15 \times 15$ ,  $20 \times 20$ ,  $25 \times 25$ , and  $30 \times 30$  voxels, and then around the size having given the best results,  $30 \times 30$ , namely from  $26 \times 26$  to  $34 \times 34$  voxels), and progressive prior noise SD,  $\sigma_i = \sigma_l + 100 * i$  for  $i \in \{-2, -1, 0, 1, \dots, 20\}$ , with  $\sigma_l = 242.91$ . From  $\sigma_i = 242.91$  (aROI4) to  $\sigma_i = 442.91$  (others ROIs) and for all window sizes, BOLD detection was effective. Again, we observed that the best-detected BOLD areas were statistically obtained using denoising parameters that introduced the strongest low-pass filters. The largest subregions (around a window size of  $30 \times 30$  voxels) and very high values of  $\sigma_i$  gave the best spatial correlations: from  $\sigma_i = 642.91$  (aROI3), to  $\sigma_i = 842.91$  (aROI1 and aROI2) and to  $\sigma_i = 1142.91$  (aROI4) (Fig. 3b). Finally, we applied wavelet-based denoising techniques using a coefficient thresholding approach. Both shrinkage methods with all available decomposition levels (1 to 6), a broad panel of spline degrees (from 0 to 5) and progressive coefficient thresholding (from 5 to 55), were applied. The best results were obtained using soft thresholding with high threshold values and levels of wavelet decomposition (3 and 4), which correspond to denoising parameters that produce a low-pass filtering function (Fig. 3b); “smoothness” orders were equivalent for the optimal detection of the four ROIs.

The above results demonstrate the utility of prior ICA denoising when the data are badly degraded by noise for which Gaussian smoothing and, to the nearly same extent, wavelet-based filtering methods seem particularly adapted. Otherwise, oversmoothing parameters were needed to optimize the ICA performance, whereas the opposite was observed for spatial SNR maximization; it is noteworthy that the ICA performances tended to plateau with progressive oversmoothing strength regardless of the denoising methods.

For aROI1, aROI3 and aROI4, Gaussian smoothing and the non-stationary Gaussian method achieved maximal BOLD region detection with filtering parameters providing equivalent “smoothness” orders, while the wavelet thresholding technique needed parameters performing higher smoothing strength. In contrast, the non-stationary Gaussian method allowed a better detection of aROI2 for a lower “smoothness” order in comparison to the other methods. When compared to the others ROIs, aROI3 needed less smoothing strength to be outlined with highest precision in terms of spatial correlation (Fig. 4). Finally, aROI4, which yielded a sinusoid signal of low frequency, benefited substantially from prior denoising and showed little sensitivity to the denoising strength of the various filters (Fig. 4). However, the detected time course was not significantly correlated to its initial HRF.

**4.2.2.2. Artificial data with a SNR of 20 dB.** As for the previous section, best results for all denoising methods compared to no prior denoising, are summarized in Table 2.

Applied to the noisy data without prior filtering, ICA enabled visual detection of aROI4; albeit spatial correlation of aROI2 and aROI3 was significant, only few voxels within these areas could be visually identified and the sensitivity remained extremely low for both regions; however, the correlation of the ICA time courses of all aROIs was significant (Fig. 3c).

As for the previous set of synthetic data, denoising significantly improved the ICA. Gaussian smoothing was applied with progressive FWHM values from 4 to 14 mm. All Gaussian kernel widths yielded well-delimited BOLD areas, even with very low FWHM. However, optimal ICA detection of ROI1 was achieved for higher FWHM values; probably the Gaussian kernel had to cover a higher surface of the BOLD area, as the latter could not be outlined by ICA without prior denoising (Fig. 3c). For non-stationary Gaussian modelling, we applied the same subregion sizes as above and a progressive prior noise SD of  $\sigma_i = \sigma_l + 50 *$

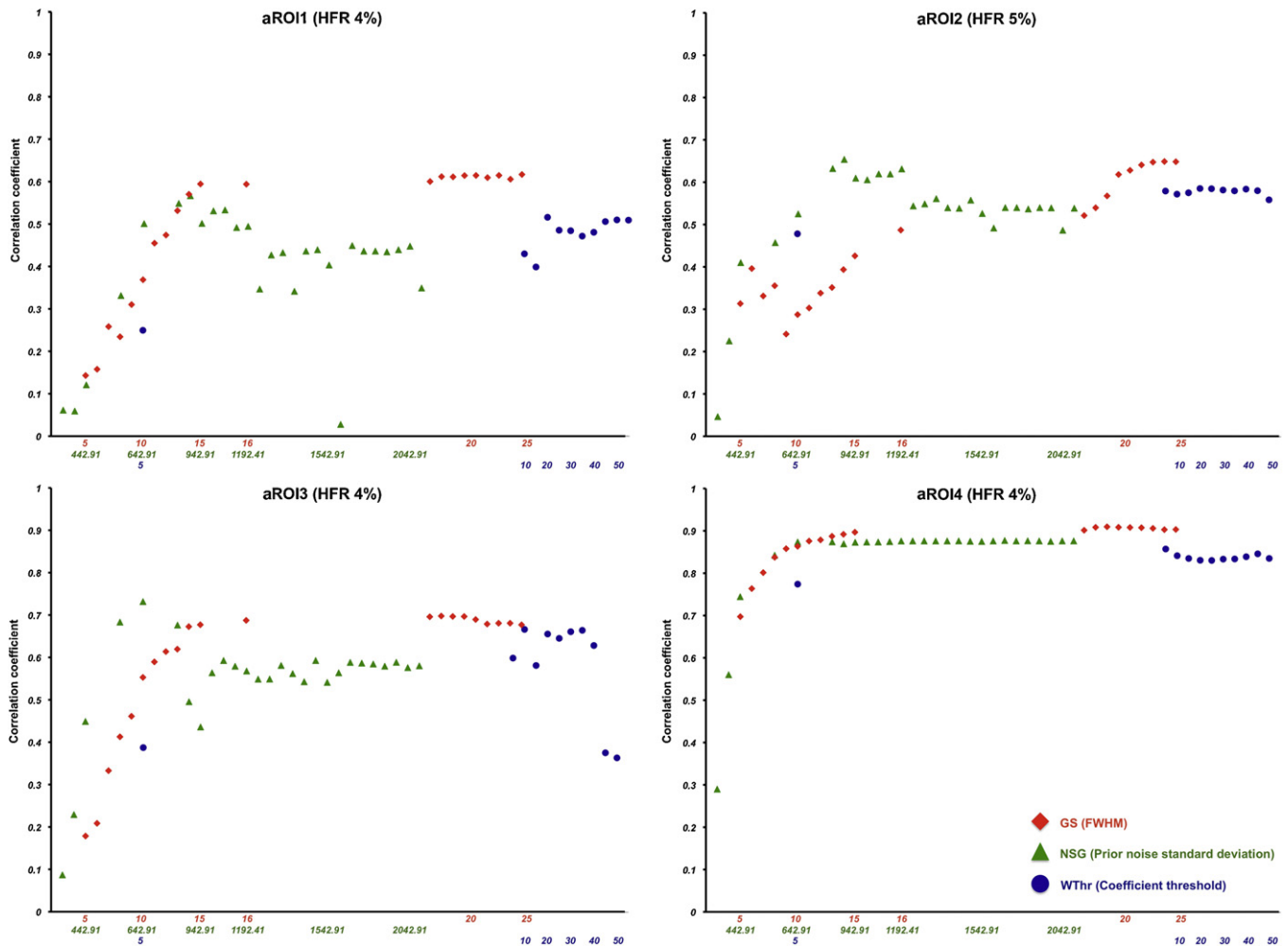


**Fig. 4.** ICA performance after denoising, for data degraded by a Rician noise of 10 dB. The coefficient of spatial correlation (Y-axis) between the BOLD mask and the best activation maps (FDR correction) for each aROI (aROI1, top left; aROI2, top right; aROI3, bottom left; aROI4, bottom right) is plotted against the filtering parameters: the FWHM of the Gaussian smoothing kernel (red diamond and first X-axis in red), the prior noise SD used for the non-stationary Gaussian modelling (green triangle and second X-axis in green), and the values used to perform soft thresholding of wavelet coefficients (blue circle and third X-axis in blue). Criteria of “smoothness” equivalence (SNR and mean square error) were used to fit all X-axis and chart titles contain the indication of the HRF increase rate against the baseline (BOLD: blood oxygen level-dependent; aROI: region of interest in the artificial data; FWHM: full width at half maximum; SD: standard deviation; GS: Gaussian smoothing; NSG: non-stationary Gaussian; WThr: thresholding of wavelet coefficients; HRF: haemodynamic response function). (For interpretation of the references to colour in this figure legend, the reader is referred to the web version of the article.)

$i$  for  $i \in \{-1, 0, 1, \dots, 10\}$ , where  $\sigma_i$  was the calculated SD of the noise ( $\sigma_i = 76.81$ ). Better BOLD detection with significant correlation was effective for all denoising parameters, except for aROI1 that was outlined with higher low-pass filtering parameters ( $\sigma_i \geq 226.81$ ) (Fig. 3c). Finally, the wavelet method based on its coefficients thresholding produced practically similar effects on the ICA. We used both shrinkage methods with all available decomposition levels (1–6), a broad panel of spline degrees (from 0 to 5) and progressive coefficient thresholding (from 2 to 98). Best ROIs detection was achieved for soft shrinkage, but with a level of wavelet decomposition reduced to 2–3 (Fig. 3c).

As observed in the data corrupted by the higher level of noise (10dB), prior filtering was also useful for analysis of slightly degraded images and all methods provided optimal results when parameters were set to effectively perform low-pass filtering; basic denoising through Gaussian smoothing gave globally the best results, whereas the performance of both of the wavelet methods came very close to Gaussian smoothing.

The filtering parameters differed from those needed to maximize the spatial SNR.

This statement can be illustrated quantitatively with the results of the non-stationary Gaussian method and its denoising parameters used to optimize ICA: the smoothing parameters inserted a higher noise variance-optimized ICA ( $\sigma_i \geq 376.81$ ) determining a “smoothness” order equivalent to the one given by a FWHM  $\geq 5$  in Gaussian smoothing, whereas a maximal SNR required a close approximation of the true noise variance ( $\sigma_i \cong 76.81$ ). Data corrupted by lower noise levels requires less smoothing strength allowing some preservation of the image information at high frequencies, although ICA performances tended to plateau with higher smoothing strengths.

For all ROIs, Gaussian smoothing and the non-stationary Gaussian technique achieved maximal BOLD region detection with filtering parameters providing equivalent “smoothness” orders, while higher smoothing strength were needed for wavelet thresholding (Fig. 5). As seen for the previous data set, aROI4 remained substantially sensitive to prior denoising and showed little sensitivity to the denoising strength of the various filters (Fig. 5), but the detected time course remained significantly uncorrelated to its true HRF.

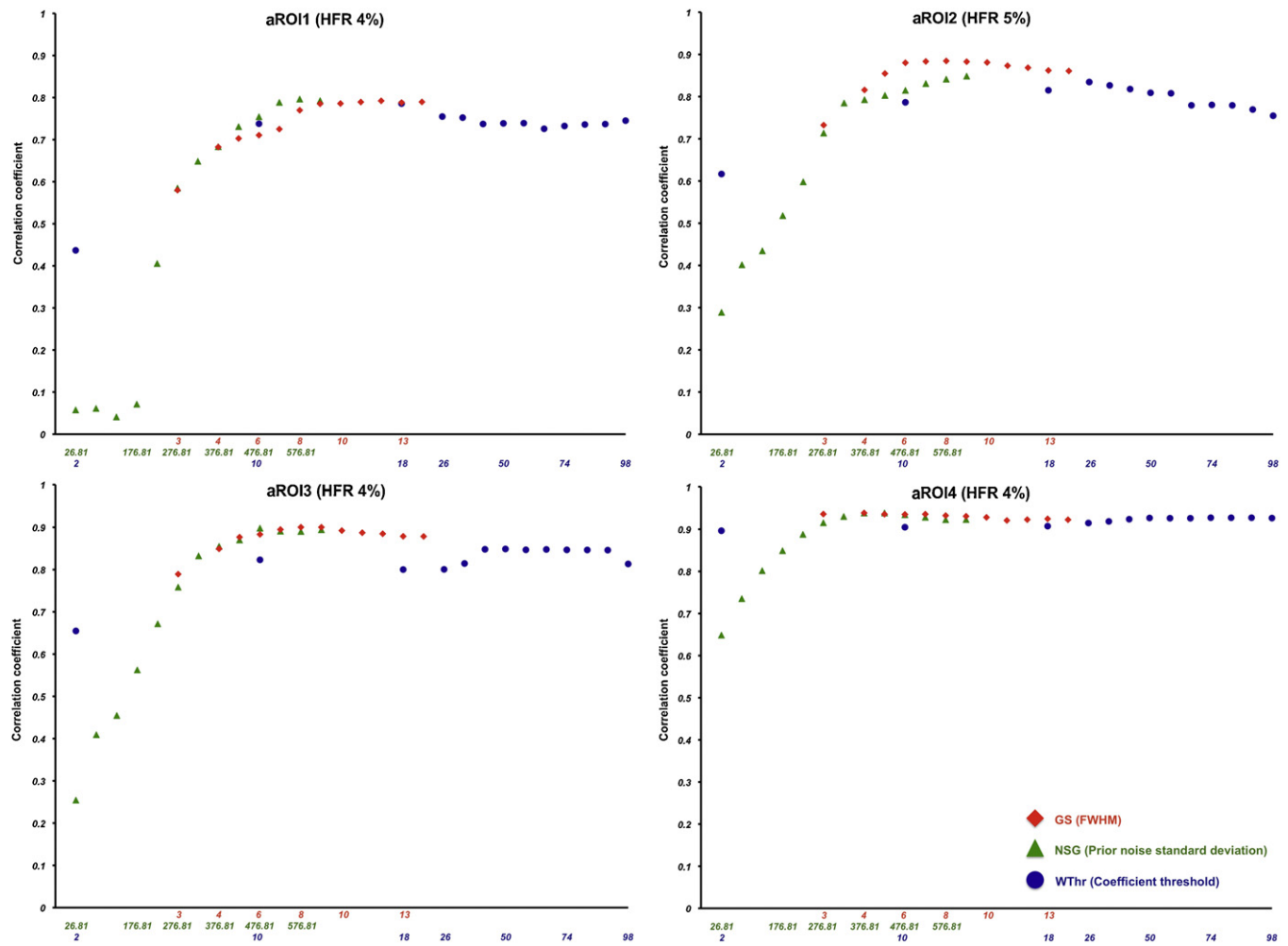


**Fig. 5.** ICA performance after denoising, for data degraded by a Rician noise of 20 dB. The coefficient of spatial correlation (Y-axis) between the BOLD mask and the best activation maps (FDR correction) for each aROI (aROI1, top left; aROI2, top right; aROI3, bottom left; aROI4, bottom right) is plotted against the filtering parameters: the FWHM of the Gaussian smoothing kernel (red diamond and first X-axis in red), the prior noise SD used for the non-stationary Gaussian modelling (green triangle and second X-axis in green), and the values used to perform soft thresholding of wavelet coefficients (blue circle and third X-axis in blue). Criteria of “smoothness” equivalence (SNR and mean square error) were used to fit all X-axis and chart titles contain the indication of the HRF increase rate against the baseline (BOLD: blood oxygen level-dependent; aROI: region of interest in the artificial data; FWHM: full width at half maximum; SD: standard deviation; GS: Gaussian smoothing; NSG: non-stationary Gaussian; WThr: thresholding of wavelet coefficients; HRF: haemodynamic response function). (For interpretation of the references to colour in this figure legend, the reader is referred to the web version of the article.)

### 4.3. Hybrid data

As previously, Table 3 presents in details best results for all denoising methods with regard to their optimal filtering parameters, and compared to no prior denoising.

As for the artificial data, the specificity will not be presented, due to its non-contributory values ( $Sp > 0.97$ ) in all conditions.

Although some BOLD regions could be partially outlined in ICA components for a significance level of 0.05 (Fig. 6a), ICA could not isolate, after FDR correction, any BOLD region (Fig. 6b), in terms of correlation coefficient and sensitivity. However, prior denoising ameliorated significantly the results (Fig. 6b). Gaussian smoothing outlined the BOLD regions for progressive FWHM values starting from 3 mm for hROI2 and hROI4, from 4 mm for hROI1 and from 5 mm for hROI3. Non-Gaussian modelling in the wavelet domain was then applied using the same subregion sizes as previously described and progressive prior noise SD starting from 20,  $\sigma = 20 + 20 * i$  for  $i \in \{0, 1, 2, \dots, 11\}$ . SD exceeding 80 produced systematic detection of the BOLD regions (SD of 60 for hROI4 and SD of 80 for hROI1 and hROI2), except for hROI3 that needed more low-pass filtering strength with a high SD of 260. Finally,

wavelet-based denoising using thresholding was performed. We applied both shrinkage methods with progressive decomposition levels (1–5) and the usual panel of spline degrees (from 0 to 5). Hard shrinkage, with parameters set to 2 (others ROIs) and 3 (hROI1) for the level decomposition yielded the best correlations and sensitivities. The use of very high coefficients thresholding reflected the necessity of strong low-pass filtering to optimize the ICA results; however, highest thresholding values were needed to obtain best detection of hROI3.

As observed in the artificial data, denoising enhanced the BOLD region detection and low-pass filtering maximized ICA performances. Basic smoothing, represented by the classic Gaussian smoothing, provided equivalent results compared to both wavelet-based methods. Albeit “smoothness” orders could not be compared between the different denoising methods in the absence of SNR measures, it is noteworthy that for all filtering techniques, optimal detection of hROI3 (HRF of lowest amplitude) required filtering parameters rendering higher smoothing strength in comparison to the other ROIs (Fig. 7). Finally, ICA results concerning hROI4 remained similar to those obtained for aROI4: it was substantially sensitive to prior denoising, it had little sensitivity to denoising

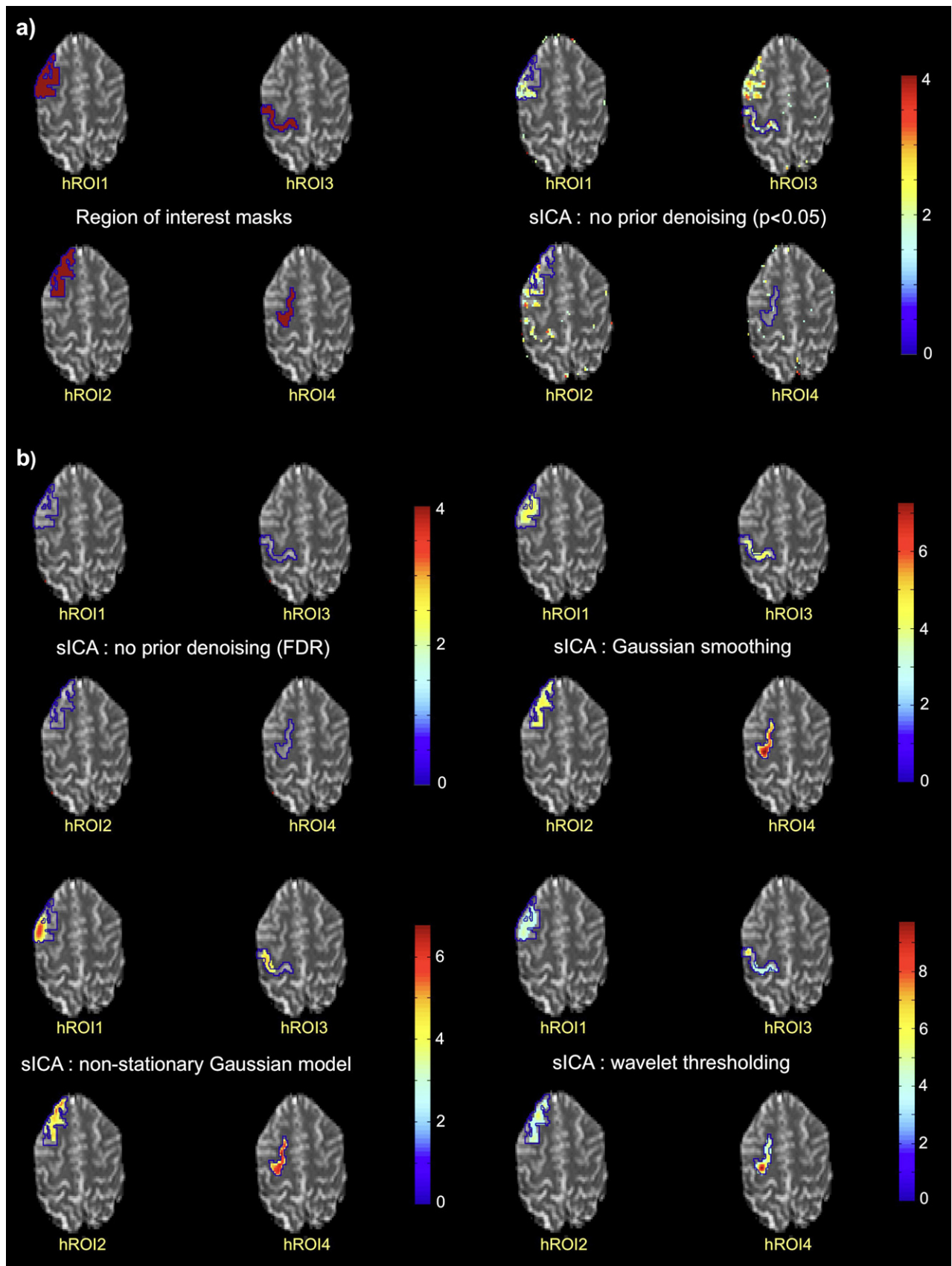


**Fig. 6.** (a) The hybrid data with the selected BOLD ROIs shown in red (left); the sICA activation maps from the hybrid data without preprocessing for a significance level of 0.05 (right) and (b) after FDR correction (top left). (b) Best sICA activation maps from the hybrid data after denoising (FDR correction): Gaussian smoothing (top right), filtering with non-stationary Gaussian modelling in the wavelet domain (bottom left), and wavelet denoising by hard thresholding (bottom right). The associated filtering parameters are detailed in Tables 1 and 2 (BOLD: blood oxygen level-dependent; hROI: region of interest in the hybrid data; sICA: spatial independent component analysis; FDR: false discovery rate). (For interpretation of the references to colour in this figure legend, the reader is referred to the web version of the article.)

**Table 3**

Summary of the best statistical ICA performances in terms of spatial correlation and sensitivity after FDR correction, shown for all hROIs of the hybrid data. Inclusion of the sensitivity and of the correlation coefficient that are related to the best spatial correlation and sensitivity respectively. Best result for each hROI is outlined in red and in italic.

	<i>Denoising methods</i>	<i>Filtering parameters</i>	<i>Correlation (FDR)</i>	<i>Related sensitivity</i>	<i>Time correlation</i>	<i>Filtering parameters</i>	<i>Sensitivity (FDR)</i>	<i>Related correlation</i>	<i>Time correlation</i>
<i>hROI1</i>	<i>No denoising</i>		<0.1				<0.1		
	<i>GS</i>	<i>FWHM</i> 12	0.59 (3.5)	0.42	0.61	12	0.42 (3.50)	0.59	0.61
	<i>NSGM</i>	<i>Window size</i> 26,28 <i>Prior noise SD</i> 480,500	0.60 (5.54-3.55)	0.39	0.89	26,28 480,500	0.39 (3.54-3.57)	0.60	0.89
	<i>WThr</i>	<i>Spline degree</i> 2 <i>Level decomp</i> 3 <i>Threshold</i> 600000	0.64 (3.47)	0.48	0.62	2 3 600000	0.48 (3.47)	0.64	0.62
	<i>No denoising</i>		<0.1				<0.1		
<i>hROI2</i>	<i>GS</i>	<i>FWHM</i> 5	0.70 (3.55)	0.49	0.78	7,8,9	0.50 (3.46-3.48)	0.67	0.82
	<i>NSGM</i>	<i>Window size</i> 26 <i>Prior noise SD</i> 200	0.69 (3.50)	0.49	0.81	26 200	0.49 (3.50)	0.69	0.81
	<i>WThr</i>	<i>Spline degree</i> 3 <i>Level decomp</i> 2 <i>Threshold</i> 260000,500000	0.69 (3.47)	0.52	0.82	4 2 95000	0.54 (3.48)	0.68	0.92
	<i>No denoising</i>		<0.1				<0.1		
	<i>GS</i>	<i>FWHM</i> 10	0.56 (3.71)	0.39	0.79	10,11	0.39 (3.66-3.71)	0.56	0.79
<i>hROI3</i>	<i>NSGM</i>	<i>Window size</i> 26,28,30 <i>Prior noise SD</i> 400,460-500	0.50 (3.67-3.70)	0.33-0.34	0.75	26,28 460-500	0.35 (3.68-3.74)	0.50	0.75
	<i>WThr</i>	<i>Spline degree</i> 2,4 <i>Level decomp</i> 2 <i>Threshold</i> 105000,95000	0.59 (3.69,3.73)	0.43-0.39	0.84	2 2 105000	0.43 (3.70)	0.59	0.84
	<i>No denoising</i>		<0.1				<0.1		
	<i>GS</i>	<i>FWHM</i> 4,5	0.91 (3.54-3.54)	0.86	<0.1	4,5	0.86 (3.55-3.59)	0.91	<0.1
	<i>NSGM</i>	<i>Window size</i> 26-34 <i>Prior noise SD</i> 60,80	0.89 (3.56-3.69)	0.82	<0.1	26-34 60,80	0.82 (3.56-3.69)	0.89	<0.1
<i>hROI4</i>	<i>WThr</i>	<i>Spline degree</i> 3,4 <i>Level decomp</i> 2 <i>Threshold</i> 440000,100000	0.85 (3.55-3.58)	0.82	<0.1	3,4 2 440000,100000	0.82 (3.53-3.55)	0.85	<0.1

(FDR: false discovery rate; hROI: region of interest in the hybrid data; GS: Gaussian smoothing; NSGM: non-stationary Gaussian modelling; WThr: thresholding of wavelet coefficients; FWHM: full width at half maximum; SD: standard deviation).

strength variations (Fig. 7) and the detected time course was significantly uncorrelated to its true HRF.

## 5. Discussion

ICA is an elegant multivariate method that allows extraction of temporally coherent network from fMRI data without being constrained by prior assumptions about timing or haemodynamic features. Because ICA also identifies the noisy components of the data, it can be considered as a filtering technique for isolating the most neurologically relevant components. However, practice has shown that prior data denoising improves ICA results. Two reasons may motivate such prior filtering. (1) Noise removal improves estimation of the demixing matrix during ICA. (2) Strengthening the assumed smoothness of BOLD sources by data smoothing may increase the independence of the sources by maximizing their uniform distribution, which leads to a higher joint entropy. In the context of ICA, one may state that the purpose of prior filtering is to reduce noise while increasing the independence between the components.

Among the denoising methods used in neuroimaging analysis, Gaussian smoothing is commonly applied and acts as a classical low-pass filter with strong noise-reduction properties. Enhanced independence may be achieved by increasing the source smoothness. However, smoothing removes high frequency information, which reduces source independence. Thus, we compared Gaussian smoothing with more sophisticated denoising methods that reduce less the information held in high-frequency signals such as borders and edges. We hypothesized that wavelet-based filters and our proposed non-stationary Gaussian modelling in the wavelet domain would yield better results because they efficiently improved both the SNR and the source independence.

We generated fMRI artificial data yielding several regions of interest with different haemodynamic functions, which were then corrupted by two different noise levels. The first data set was parameterized such that the ICA was not able to isolate the independent task-related components from the raw data. To approach real fMRI conditions and to validate previous ICA results with synthetic data, hybrid data were created in the same way as the artificial data: the same theoretical haemodynamic functions were added to defined BOLD regions from real fMRI images acquired during a resting task. Various statistical criteria were then applied to link the statistical activation maps, with the BOLD mask.

After we demonstrated analytically the applicability of prior denoising to ICA, we confirmed that both wavelet-based denoising methods performed better in terms of the SNR compared to classical Gaussian smoothing, whereas the best results were recorded using a novel wavelet denoising techniques based on a non-stationary Gaussian modelling within the Bayesian framework.

Three key observations can be deduced from the ICA results after filtering of both artificial and hybrid data, using spatial correlation as the principal quality measure, and sensitivity:

1. It was empirically demonstrated that prior denoising improved ICA results.
2. All filtering techniques were effective, and their performances were equivalent from method to method regardless of the noise grade or of the data type (artificial versus hybrid); indeed, the differences in the results between ROIs, HRF and data type, were heterogeneous and not sufficiently significant to define a superior filtering method.
3. The values of the denoising parameters that maximized the spatial SNR resulted into filters that mainly acted like low-pass filters with oversmoothing; it is noteworthy that the smoothing

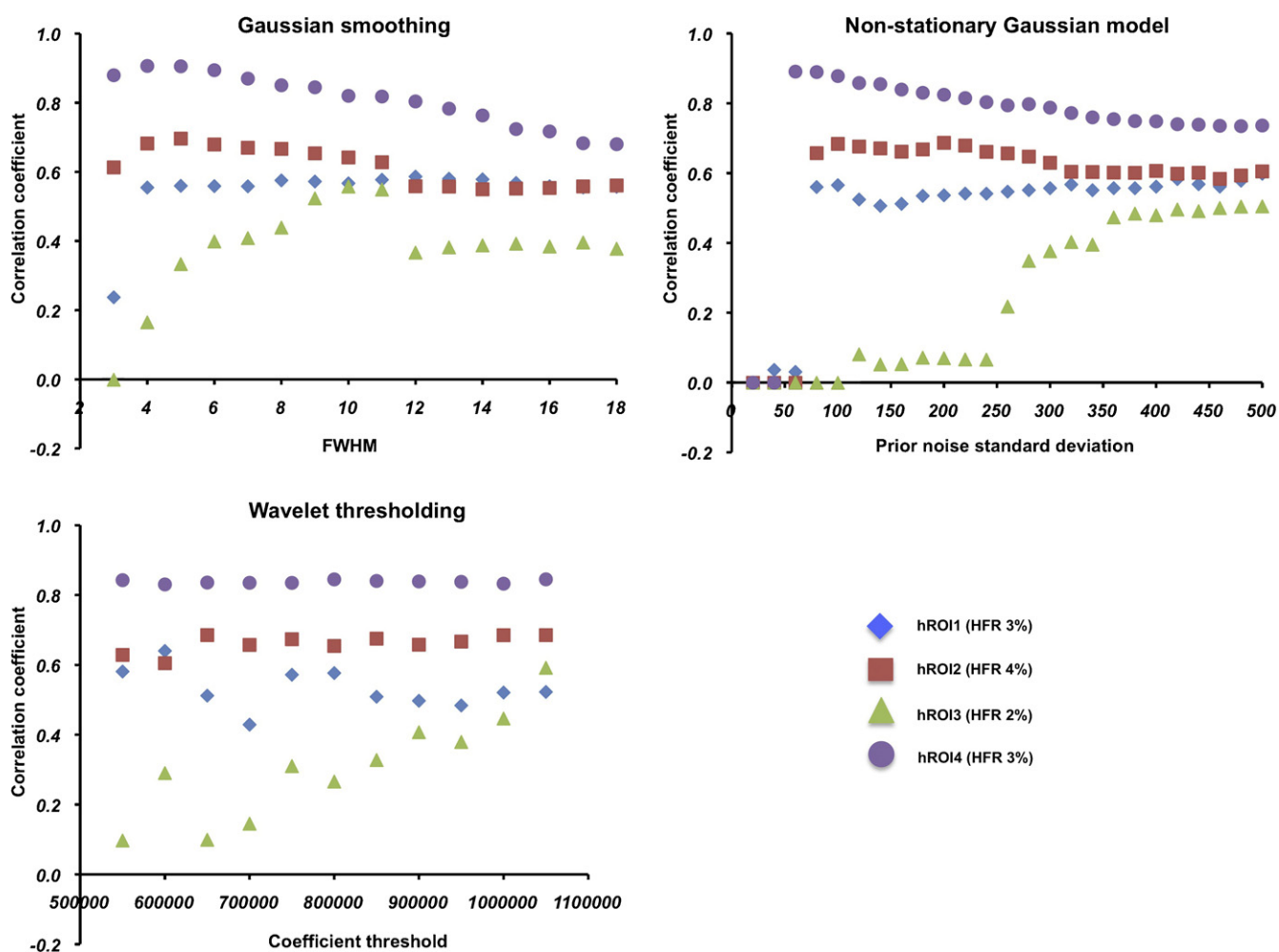


**Fig. 7.** ICA performance after denoising, for hybrid data. The coefficient of spatial correlation (Y-axis) between the BOLD mask and the best activation maps (FDR correction) of each hROI (hROI1, black diamond; hROI2, red square; hROI3, green triangle; hROI4, violet circle) is plotted against the filtering parameters (X-axis): the FWHM of the Gaussian smoothing kernel (top left), the prior noise SD used for the non-stationary Gaussian modelling (top right), and the values used to perform hard thresholding of wavelet coefficients (bottom left). Chart legend contains the indication of the HRF increase rate against the baseline for each hROI (BOLD: blood oxygen level-dependent; FWHM: full width at half maximum; SD: standard deviation; hROI: region of interest in the hybrid data; HRF: haemodynamic response function). (For interpretation of the references to colour in this figure legend, the reader is referred to the web version of the article.)

strength seemed to be correlated with the noise level or the amplitude of the time course signal: low SNR or low HRF amplitude needed higher smoothing strength. Besides, detection of ROIs yielding a sinusoid function of low frequency mimicking a resting-state activity is much more sensitive to prior denoising and is already effective for slight smoothing.

The last observation can also be interpreted as follows. Strong smoothing enhances the Gaussianity of the data as predicted by the central limit theorem, leading in theory to a reduced performance of ICA due to less non-Gaussianity in the data. Several hypotheses may be advanced to explain why low-pass filtering improves ICA, whereas the filtering parameters that produced the best denoising, in terms of SNR, did not consistently improve ICA results. The results suggest that some image components are more involved in ICA performance.

Regardless of its energy, noise plays a significant role in ICA because strong reductions in noise due to low-pass filtering determine ICA performance. We showed that the smoothing strength tended to be proportional to the noise intensity or to the HRF amplitude: badly degraded data or low signal amplitude required oversmoothing to provide the best ICA, whereas mild smoothing was sufficient for data corrupted by lower noise or for higher

amplitude. Otherwise, smoothing may contribute to increasing the independence of sources to a certain extent. Indeed, because BOLD sources are assumed to be smooth, an increase in smoothness produces uniformity in the statistical distribution of the sources, leading to higher joint entropy.

By contrast, image information embedded in the high frequencies did not seem to play a main role in ICA, because smoothing eliminates this information. It is interesting to note that recent work (Chialvo et al., 2008) has shown that resting-state fMRI exhibits scale-free spatial organization, which means that similar patterns are recovered at different spatial scales, but the coarse scales might be easier to reveal in a noisy context (after Gaussian smoothing).

Accordingly, the initial hypothesis that band-pass filtering during preprocessing should be superior to low-pass filtering should be challenged and the question arises why more sophisticated wavelet-based methods with powerful denoising characteristics did not improve more efficiency in ICA, than basic smoothing, at least according to the spatial correlation or sensitivity criteria. A first explanation may be based on the fact that wavelet denoisers introduce non-linearities in the data lowering in this way the ICA efficiency. Secondly, the criterion of spatial correlation is applied after thresholding, which removes some of the typical artefacts

encountered with Gaussian smoothing, such as poor shapes of activation. However, the outcome of ICA is mostly assessed by considering “suprathresholded” voxels, which are the ones characterized by our criterion. Thirdly, SNR improvement and ICA are two different steps in fMRI signal processing because denoising and detection are, themselves, distinct processes. Computed disjointly, both procedures may render individually optimal results, but it is not necessarily the case when both procedures are combined. Information from one process may influence the other. Here, denoising preceded detection such that statistical changes had the potential for hampering the detection power. For example, the lower influence of the powerful wavelet-based filtering on ICA may result from excessive statistical changes that may not occur under Gaussian smoothing. Accordingly, in the context of the feature-selective scheme (Li et al., 2007), ICA or other detection methods may be designed to exploit the strength of the best denoising techniques: Khullar demonstrated this by designing an ICA method that operated in the wavelet domain, and which performance was better than those obtained with prior Gaussian smoothing in the image domain (Khullar et al., 2011).

Finally, we can advance an additional benefit of spatial smoothing related to the application of ICA to group studies. Indeed, inter-subject variability, which is hindering even after normalizing the subject to the same space, is certainly decreased by spatial smoothing; we refer to Allen et al. (2012) for a detailed analysis of this issue.

## 6. Conclusion

We confirmed that prior denoising by performing low-pass filtering is beneficial and in some cases even essential for ICA to work properly. Compared to wavelet-based filtering methods, simple and computationally efficient Gaussian smoothing provides equivalent performance according to spatial correlation and sensitivity criteria of the recovered maps. Nevertheless, wavelet methods, such non-stationary Gaussian modelling, may represent an interesting compromise between ICA improvement and the best spatial noise reduction in terms of SNR. This approach should be tested by integration into ICA for the purposes of potentiating its properties.

## Conflict of interest

None of the authors have any conflicts of interest to disclose.

## Acknowledgments

This study was supported by the Swiss National Sciences Foundation (Grants 31-59516 and PP00P2-123438), by the de Reuter Foundation, by the Ernst & Lucie Schmidheiny Foundation, and by the Academic Society of Geneva. It was also supported by the Center for Biomedical Imaging (CIBM) of the Geneva and Lausanne Universities, the EPFL and the Geneva and Lausanne University Hospitals. We express also our gratitude to Prof. Theodor Landis for his support.

## Appendix A.

### A.1. Maximum a posteriori probability image de-noising

Since in MR images the distribution of Rician noise follows a Gaussian distribution, the original fMRI image, noted  $X$ , is degraded by additive white Gaussian noise (AWGN),  $Z$ :

$$Y = X + Z; \quad (A1)$$

where  $Y$  is the acquired fMRI image and  $Z \sim N(0, C_Z)$  an i.i.d. AWGN zero-mean with a known co-variance matrix  $C_Z$ .

With available proper prior information,  $X$  is estimated from its corrupted version  $Y$ , in performing a maximum a posteriori (MAP) estimation:

$$\hat{x} = \arg \max_{x \in \mathbb{R}^N} (p_{Y|X}(y|x)p_x(x)), \quad (A2)$$

where  $\hat{x}$  is the estimate of  $X$ ,  $p_{Y|X}(y|x)$  the likelihood function for the AWGN and finally,  $p_x(x)$  the prior distribution of the original image.

As image and noise are assumed to be multivariate Gaussian, i.e.  $X \sim N(\bar{x}, C_X)$  and  $Z \sim N(0, C_Z)$ , the solution of estimation (A2) becomes:

$$\hat{x} = C_Z(C_Z + C_X)^{-1}\bar{x} + C_X(C_Z + C_X)^{-1}y. \quad (A3)$$

Since the MAP estimator is linear, the estimation error  $\tilde{x} = \hat{x} - x$ , remains Gaussian  $\tilde{X} \sim N(0, C_Z)$ , and its covariance matrix is defined as:

$$C_{\tilde{X}} = C_X(C_Z + C_X)^{-1}C_Z; \quad (A4)$$

besides, the variance of the MAP estimator is:

$$\hat{\sigma}_{\tilde{X}}^2 = \frac{1}{N} \text{Tr}(C_{\tilde{X}}). \quad (A5)$$

If  $X$  remains uncorrelated but becomes non-stationary,  $C_X = \text{diag}(\sigma_X^2(1), \sigma_X^2(2), \dots, \sigma_X^2(N))$  with the assumption that the noise, is AWGN,  $C_Z = \sigma_Z^2 I_N$ , the MAP estimator of  $X$  can be written as followed:

$$\hat{x}(i) = \bar{x}(i) + \frac{\sigma_X^2(i)}{\sigma_X^2(i) + \sigma_Z^2} (y(i) + \bar{x}(i)) \quad (A6)$$

with variance:

$$\hat{\sigma}(i) = \bar{x}(i) + \frac{\sigma_X^2}{\sigma_X^2 + \sigma_Z^2} (y(i) + \bar{x}(i)). \quad (A7)$$

If additionally  $X$  becomes white Gaussian,  $C_X = \sigma_X^2 I_N$ , the MAP estimator of  $x$  is one-to-one mapping;

$$\hat{x}(i) = \bar{x}(i) + \frac{\sigma_X^2}{\sigma_X^2 + \sigma_Z^2} (y(i) + \bar{x}(i)), \quad (A8)$$

and its variance is:

$$\hat{\sigma}_{\tilde{X}}^2 = \frac{\sigma_X^2 \sigma_Z^2}{\sigma_X^2 + \sigma_Z^2}, \quad (A9)$$

To analyze the non-stationary Gaussian data case, the local variance estimate should be assessed by applying a maximum likelihood (ML) method, as local stationarity, is assumed:

$$\hat{\sigma}_{\tilde{X}}^2(i) = \frac{1}{|\Omega|} \sum_{k \in \Omega(i)} (x(k) - \bar{x}(i))^2, \quad (A10)$$

where  $\Omega(i)$  is a square window centred at  $x(i)$  with  $|\Omega|$  the cardinality of  $\Omega(i)$  and  $\bar{x}(i)$  the local mean of  $\Omega(i)$ :

$$\bar{x}(i) = \frac{1}{|\Omega|} \sum_{k \in \Omega(i)} x(k). \quad (A11)$$

Modelling principle based on geometrical prior information in wavelet domain

Real  $X$  images are non-stationary but if we assume that they are composed by a number of statistically homogenous regions in the coordinate domain, each region may be modelled as stationary Gaussian with some variance (Wilson, 1999). In this case, classical ML estimators lead to over-estimation of the local variance, which

can be avoided by considering  $X$  as a union of non-overlapping regions  $R_i$  with i.i.d. Gaussian statistics:

$$\cup_i R_i = S; R_i \cap R_j = \emptyset, \quad (A12)$$

with  $i = 1, 2, \dots, n$ , and where  $S$  is the initial support of  $X$ .

Thus, variance is only estimated in the corresponding sub-region  $R_i$ , and the classical ML estimate can be replaced by a restricted support ML local variance estimate:

$$\hat{\sigma}_X^2(i) = \frac{1}{|\Omega|} \sum_{k \in \Omega(i)} x(k)^2 m_k, \quad (A13)$$

$|\Omega|$  is the cardinality of the subset  $\Omega$  and  $m_k$  is a subset indicator function:

$$m_k = \begin{cases} 1, & k \in \Omega, \\ 0, & \text{otherwise.} \end{cases} \quad (A14)$$

As denoising is more efficient in the wavelet domain, partition technique of regions and adaptive ML method are performed in the transform domain. To overcome the Gibbs phenomenon in borders (edges) of the reconstructed image, non-decimated wavelet transform without downsampling is applied (Chrysafis, 2000). Voloshynovskiy et al. has shown that best results were obtained with 9/7 CDF biorthogonal filter pair and 4 levels of decomposition (Voloshynovskiy et al., 2005). Since variance distribution of the wavelet coefficients in high frequency subbands is close to a Rayleigh distribution, the MAP estimate can be used instead of the ML estimate for the local variance:

$$\sigma_{MAP}^2 = \frac{s^2(|M| - 1)}{2} \left[ -1 + \sqrt{1 + \frac{4}{s^2(|M| - 1)} \sum_{i=1}^{|M|} (x(i)^2)} \right], \quad (A15)$$

with  $|M|$  the cardinality of the sampling window and  $s$  the scalar parameter estimated in each subband calculated with the ML estimation in a sampling window of dimension  $d$ :

$$s^2 = \frac{1}{2N} \sum_{k \in \Omega(i)} \sigma_{dxd}^2(i). \quad (A16)$$

## A.2. Edge process model

To overcome computational complexity that results from the consideration of the local information in the stochastic image, edge process modelling was developed (Voloshynovskiy et al., 2005). Since no linear transform is able to decorrelate completely the edges, the residual correlation of the image remains in the high frequency subbands. Performance can be improved with additional decorrelation, by subtracting edges from the high frequency subband data that allows local variance reduction and that leads to locally Gaussian distribution.

Concretely, the image,  $X$ , is decomposed in non-decimated subbands that have each their own support  $S_l$ , with  $l = 1, \dots, 3W$ , where  $W$  is the number of dyadic decomposition level such that  $S_i \cap S_j = \emptyset, i \neq j$  and  $\cup_l S_l = S$ . Edge process model assumes that each subband is separated in two distinctive sets of wavelet coefficients corresponding to the flat region  $R_1$  and to edge and texture region  $R_2$ , respectively, which are statistically defined as:

$$R_1 = \{x : X(i) \sim N(0, \sigma_X^2(i))\}, \quad (A17)$$

$$R_2 = \{x : X_j(i) \sim N(\bar{x}_j(i), \sigma_{X_j}^2(i))\}, \quad (A18)$$

where  $R_1 \cup R_2 = S$ .  $R_1$  is assumed to be zero-mean Gaussian with the local variance  $\sigma_X^2(i)$ . Within  $R_2$ , each distinct geometrical structure that corresponds to an edge or a texture transition is decomposed into a set of local means. Besides, a particular mean  $\bar{x}_j(i), j = 1, \dots, J$  of the different structure propagates along the edge corresponding

to the edge subtraction strategy, the so-called *edge process (EP)*. Thus, the coefficient on the edge regions may have a possible value from the set  $\{\bar{x}_j(i)\}$ , such that the coefficients variation remains small. Thus, the image may be considered as a set of flat regions that are assumed to be i.i.d. stationary Gaussian and whose wavelet subbands have low variance. Hence, EP model belongs to the Gaussian family of distribution with only difference in the estimation of model parameters. In this case, the estimation is in the form of Wiener with estimator variance:

$$\sigma_{MAP}^2 = \frac{1}{N} \sum_{i=1}^N \frac{\sigma_X^2(i) \sigma_Z^2}{\sigma_X^2(i) + \sigma_Z^2}, \quad (A19)$$

where  $\sigma_X^2(i)$  is the local image variance of the EP model.

## References

- Alexander ME, Baumgartner R, Summers AR, Windischberger C, Klarhoefer M, Moser E, et al. A wavelet-based method for improving signal-to-noise ratio and contrast in MR images. *Magn Reson Imaging* 2000;18(2):169–80.
- Allen EA, Erhardt EB, Wei Y, Eichele T, Calhoun VD. Capturing inter-subject variability with group independent component analysis of fMRI data: a simulation study. *Neuroimage* 2012;59:4141–59.
- Bandettini PA, Jesmanowicz A, Wong EC, Hyde JS. Processing strategies for time-course data sets in functional MRI of the human brain. *Magn Reson Med* 1993;30(2):161–73.
- Bell AJ, Sejnowski TJ. An information-maximization approach to blind separation and blind deconvolution. *Neural Comput* 1995;7(6):1129–59.
- Blu T, Unser M. The fractional spline wavelet transform: definition and implementation. In: *Proc IEEE: international conference on acoustics, speech, and signal processing*; 2000. p. 512–5.
- Buckheit JB, Donoho DL. Wavelet and reproducible research. Technical Report 474. Dept. of statistics, Stanford University, 1995.
- Bullmore ET, Brammer MJ, Rabe-Hesketh S, Curtis VA, Morris RG, Williams SC, et al. Methods for diagnosis and treatment of stimulus-correlated motion in generic brain activation studies using fMRI. *Hum Brain Mapp* 1999;7(1):38–48.
- Calhoun V, Adali T, Pearlson G. Independent component analysis applied to fMRI data: a generative model for validating results. In: *Proceedings, North Falmouth*; 2001a.
- Calhoun VD, Adali T, Pearlson GD, Pekar JJ. Spatial and temporal independent component analysis of functional MRI data containing a pair of task-related waveforms. *Hum Brain Mapp* 2001b;13(1):43–53.
- Calhoun VD, Adali T, Pekar JJ, Pearlson GD. Latency (in)sensitive ICA. Group independent component analysis of fMRI data in the temporal frequency domain. *Neuroimage* 2003;20(3):1661–9.
- Calhoun VD, Adali T, Pekar JJ. A method for comparing group fMRI data using independent component analysis: application to visual, motor and visuomotor tasks. *Magn Reson Imaging* 2004;22(9):1181–91.
- Calhoun VD, Adali T. Unmixing fMRI with independent component analysis. *IEEE Eng Med Biol Mag* 2006;25(2):79–90.
- Chialvo DR, Balenzuela P, Fraiman D, The Brain. What is critical about it? Collective dynamics: topics on competition and cooperation in the biosciences. *Am Inst Phys* 2008;1028:28–45.
- Chrysafis C. Wavelet image compression: rate distortion optimizations and complexity reduction. University of Southern California: Los Angeles; 2000.
- Comon P. Independent component analysis, a new concept? *Signal Process (Special issue on Higher-Order Statistics)* 1994;36(3):287–314.
- Cordes D, Haughton VM, Arfanakis K, Carew JD, Turski PA, Moritz CH, et al. Frequencies contributing to functional connectivity in the cerebral cortex in “resting-state” data. *AJNR – Am J Neuroradiol* 2001;22:1326–33.
- Correa N, Adali T, Calhoun VD. Performance of blind source separation algorithms for fMRI analysis using a group ICA method. *Magn Reson Imaging* 2007;25(5):684–94.
- Cover TM, Thomas JA. Elements of information theory. second ed. New Jersey: Wiley-Interscience; 2006.
- Donoho DL, Johnstone IM. Ideal denoising in an orthonormal basis chosen from a library of bases. *C R Acad Sci* 1994;319(Series A):1317–22.
- Donoho DL, Johnstone IM. Adapting to unknown smoothness by wavelet shrinkage. *J Am Stat Assoc* 1995;90:1200–24.
- Edelstein WA, Glover GH, Hardy CJ, Redington RW. The intrinsic signal-to-noise ratio in NMR imaging. *Magn Reson Med* 1986;3(4):604–18.
- Egolf EA, Kiehl KA, Calhoun VD. Group ICA of fMRI toolbox GIFT. 10th Annual meeting of the organization for human brain mapping. *Neuroimage* 2004;22:14–7.
- Eriksson J, Koivunen V. Characteristic-function-based independent component analysis. *Signal Process* 2003;83(10):2195–220.
- Eriksson J, Koivunen V. Identifiability: separability, and uniqueness of linear ICA models. *Signal Process Lett IEEE* 2004;11(7):601–4.
- Friston K, Holmes A, Worsley KJ, Poline JB, Frith CD, Frackowiak RSJ. Statistical parametric maps in functional imaging: a general linear approach. *Hum Brain Mapp* 1994;2(4):189–210.

- Friston KJ. Commentary and opinion: II. Statistical parametric mapping: ontology and current issues. *J Cereb Blood Flow Metab* 1995;15(3):361–70.
- Genovese CR, Lazar NA, Nichols T. Thresholding of statistical maps in functional neuroimaging using the false discovery rate. *Neuroimage* 2002;15(4):870–8.
- Ghugre NR, Martin M, Scadeng M, Ruffins S, Hiltner T, Pautler R, et al. Superiority of 3D wavelet-packet denoising in MR microscopy. *Magn Reson Imaging* 2003;21(8):913–21.
- Gold S, Christian B, Arndt S, Zeien G, Cizadlo T, Johnson DL, et al. Functional MRI statistical software packages: a comparative analysis. *Hum Brain Mapp* 1998;6(2):73–84.
- Gudbjartsson H, Patz S. The Rician distribution of noisy MRI data. *Magn Reson Med* 1995;34(6):910–4.
- Hilton M, Ogden T, Hattery D, Eden G, Jawerth B. Wavelet processing of functional MRI data. In: Aldroubi A, Unser M, editors. *Wavelets in biology and medicine*. CRC Press; 1996.
- Hyvärinen A, Oja E. Independent component analysis: algorithms and applications. *Neural Netw* 2000;13(4–5):411–30.
- Hyvärinen A, Karhunen J, Oja E, Haykin S. Independent component analysis. New Jersey: Wiley-Interscience; 2001. p. 481.
- Khullar S, Michael A, Correa N, Adali T, Baum SA, Calhoun VD. Wavelet-based fMRI analysis: 3-D denoising, signal separation, and validation metrics. *Neuroimage* 2011;54(4):2867–84.
- Kwan RK-S, Evans AC, Pike GB. An extensible MRI simulator for post-processing evaluation. *Lecture notes in computer science, visualization in biomedical computing (VBC'96)*, vol. 1131; 1996. pp. 135–140.
- Lange N, Strother SC, Anderson JR, Nielsen FA, Holmes AP, Kolenda T, et al. Plurality and resemblance in fMRI data analysis. *Neuroimage* 1999;10(3 Pt 1):282–303.
- Li YO, Adali T, Calhoun VD. A feature-selective independent component analysis method for functional MRI. *Int J Biomed Imaging* 2007;15635.
- Malonek D, Dirnagl U, Lindauer U, Yamada K, Kanno I, Grinvald A. Vascular imprints of neuronal activity: relationships between the dynamics of cortical blood flow, oxygenation, and volume changes following sensory stimulation. *Proc Natl Acad Sci U S A* 1997;94(26):14826–31.
- McKeown MJ, Makeig S, Brown GG, Jung TP, Kindermann SS, Bell AJ, et al. Analysis of fMRI data by blind separation into independent spatial components. *Hum Brain Mapp* 1998;6(3):160–88.
- McKeown MJ, Sejnowski TJ. Independent component analysis of fMRI data: examining the assumptions. *Hum Brain Mapp* 1998;6(5–6):368–72.
- Mitra PP, Ogawa S, Hu X, Ugurbil K. The nature of spatiotemporal changes in cerebral hemodynamics as manifested in functional magnetic resonance imaging. *Magn Reson Med* 1997;37(4):511–8.
- Moeller JR, Strother SC. A regional covariance approach to the analysis of functional patterns in positron emission tomographic data. *J Cereb Blood Flow Metab* 1991;11(2):A121–35.
- Ogawa S, Lee TM, Kay AR, Tank DW. Brain magnetic resonance imaging with contrast dependent on blood oxygenation. *Proc Natl Acad Sci U S A* 1990;87(24):9868–72.
- Pickens DR, Li Y, Morgan VL, Dawant BM. Development of computer-generated phantoms for fMRI software evaluation. *Magn Reson Imaging* 2005;23(5):653–63.
- Pignat J-M, Koval O, Voloshynovskiy S, Pun T. From non-stationary Gaussian modelling to independent component analysis: an fMRI study. In: *Lemanic – neuroscience annual meeting*; 2007.
- Pignat J-M, Voloshynovskiy S, Koval O, Ibanez V, Pun T. Non-stationary Gaussian spatio-temporal modelling of fMRI data. In: *Brain'05 & BrainPET'05, XXII International symposium on cerebral blood flow, metabolism, and function and VIth international conference on quantification of brain function with PET*; 2005.
- Rosenfeld A, Kak AC. *Digital picture processing*, vol. 2. Orlando, FL: Press A; 1982.
- Ruttimann UE, Unser M, Rawlings RR, Rio D, Ramsey NF, Mattay VS, et al. Statistical analysis of functional MRI data in the wavelet domain. *IEEE Trans Med Imaging* 1998;17(2):142–54.
- Sijbers J, den Dekker AJ, Van Audekerke J, Verhoye M, Van Dyck D. Estimation of the noise in magnitude MR images. *Magn Reson Imaging* 1998;16(1):87–90.
- Stone JV. Independent component analysis: a tutorial introduction. Massachusetts London: The MIT Press; 2004.
- Turkheimer FE, Brett M, Aston JA, Leff AP, Sargent PA, Wise RJ, et al. Statistical modelling of positron emission tomography images in wavelet space. *J Cereb Blood Flow Metab* 2000;20(11):1610–8.
- Turkheimer FE, Brett M, Visvikis D, Cunningham VJ. Multiresolution analysis of emission tomography images in the wavelet domain. *J Cereb Blood Flow Metab* 1999;19(11):1189–208.
- Unser M. Splines: a perfect fit for signal and image processing. *IEEE Signal Process Mag* 1999;16(6):22–38.
- Unser M, Blu T. Fractional splines and wavelets. *SIAM Rev* 2000;42:43–67.
- Van De Ville D, Blu T, Unser M. Integrated wavelet processing and spatial statistical testing of fMRI data. *Neuroimage* 2004;23:1472–85.
- Voloshynovskiy S, Koval O, Pun T. Image denoising based on the edge-process model. *Signal Process* 2005;85(10):1950–69.
- Wilson R. Multiresolution Gaussian mixture models: theory and applications. Research Report RR404. University of Warwick, Department of Computer Science, UK; 1999.
- Wink AM, Roerdink JB. Denoising functional MR images: a comparison of wavelet denoising and Gaussian smoothing. *IEEE Trans Med Imaging* 2004;23(3):374–87.
- Wink AM, Roerdink JBTM. BOLD noise assumptions in fMRI. *Int J Biomed Imaging* 2006;2006, 11 pages, Article ID: 12014.
- Worsley K, Marrett S, Neelin P, Evans A. Searching scale space for activation in PET images. *Hum Brain Mapp* 1996;4(1):74–90.
- Zaroubi S, Goelman G. Complex denoising of MR data via wavelet analysis: application for functional MRI. *Magn Reson Imaging* 2000;18(1):59–68.